NASA–TP–2018–220095

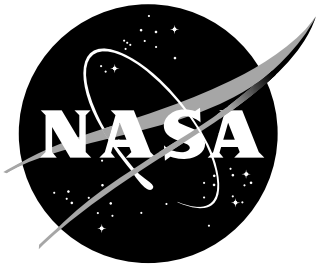

Numerically Simulating an Expanding Continuum Jet into a Surrounding Non-continuum Region

Christopher E. Glass
Langley Research Center, Hampton, Virginia

October 2018

NASA STI Program . . . in Profile

Since its founding, NASA has been dedicated to the advancement of aeronautics and space science. The NASA scientific and technical information (STI) program plays a key part in helping NASA maintain this important role.

The NASA STI program operates under the auspices of the Agency Chief Information Officer. It collects, organizes, provides for archiving, and disseminates NASA's STI. The NASA STI program provides access to the NTRS Registered and its public interface, the NASA Technical Reports Server, thus providing one of the largest collections of aeronautical and space science STI in the world. Results are published in both non-NASA channels and by NASA in the NASA STI Report Series, which includes the following report types:

- TECHNICAL PUBLICATION. Reports of completed research or a major significant phase of research that present the results of NASA Programs and include extensive data or theoretical analysis. Includes compilations of significant scientific and technical data and information deemed to be of continuing reference value. NASA counter-part of peer-reviewed formal professional papers but has less stringent limitations on manuscript length and extent of graphic presentations.

- TECHNICAL MEMORANDUM. Scientific and technical findings that are preliminary or of specialized interest, e.g., quick release reports, working papers, and bibliographies that contain minimal annotation. Does not contain extensive analysis.

- CONTRACTOR REPORT. Scientific and technical findings by NASA-sponsored contractors and grantees.

- CONFERENCE PUBLICATION. Collected papers from scientific and technical conferences, symposia, seminars, or other meetings sponsored or co-sponsored by NASA.

- SPECIAL PUBLICATION. Scientific, technical, or historical information from NASA programs, projects, and missions, often concerned with subjects having substantial public interest.

- TECHNICAL TRANSLATION. English-language translations of foreign scientific and technical material pertinent to NASA's mission.

Specialized services also include organizing and publishing research results, distributing specialized research announcements and feeds, providing information desk and personal search support, and enabling data exchange services.

For more information about the NASA STI program, see the following:

- Access the NASA STI program home page at http://www.sti.nasa.gov

- E-mail your question to help@sti.nasa.gov

- Phone the NASA STI Information Desk at 757-864-9658

- Write to:
  NASA STI Information Desk
  Mail Stop 148
  NASA Langley Research Center
  Hampton, VA 23681-2199

NASA–TP–2018–220095

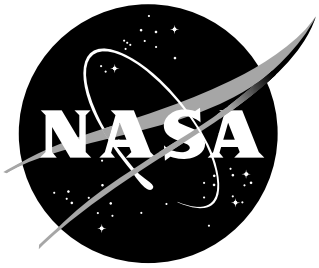

Numerically Simulating an Expanding Continuum Jet into a Surrounding Non-continuum Region

Christopher E. Glass
Langley Research Center, Hampton, Virginia

National Aeronautics and
Space Administration

Langley Research Center
Hampton, Virginia 23681-2199

October 2018

Acknowledgments

The studies presented in this document represent only a few of the many jet interaction cases, which have been simulated by DSMC. For the most part, LaRC-AB studies have been highlighted herein; however, at NASA-JSC, Dr. Forrest Lumpkin, Mr. Phillip Stuart and others have performed many critical in-orbit simulations for plume leaks and contamination for the Space Shuttle and ISS Programs and for spacecraft docking with the Mir and ISS. LaRC-AB personnel involved in DSMC jet interactions are former branch members Dr. Ditier Rault and his students Mr. Michael Woronowicz, Mr. Francisco Cestero, and Mr. Russell Shane; Dr. Dick Wilmoth, Mr. Jay LeBeau (former NASA-JSC detailee), Mr. Paul Tartabini, Dr. Jim Moss and Dr. Jose Padilla and current branch members Dr. Derek Liechty and Dr. Christopher Glass. This report was written in the LaTeX document preparation language using a modified version of the `aiaa-pretty` document class created by Dr. Derek J. Dalle.

Available from:

NASA STI Program / Mail Stop 148
NASA Langley Research Center
Hampton, VA 23681-2199
Fax: 757-864-6500

,

Table of Contents

Page

Abstract 7

Symbol List 8

1 Introduction 9

2 Uncouple Continuum and Non-continuum Jet Interaction Regions 9
2.1 Jet Interaction Flow Field . . . 9
2.2 Continuum–Non-continuum Uncoupling Surface . . . 9
2.2.1 First Approaches . . . 10
2.2.2 Bird Breakdown Parameter, P . . . 10
2.2.3 Present Technique . . . 10
2.3 Breakdown of Expanding Continuum Flow . . . 11
2.4 Application to Uncoupled CFD-DSMC Transitional Regime Jet Interaction . . . 12
2.4.1 DERA Jet Interaction Experiment . . . 12
2.4.2 General Overview of Uncoupled CFD-DSMC Jet Interaction . . . 12
2.4.3 CFD Jet Interaction Model . . . 13
2.4.4 Bird Breakdown Parameter . . . 14
2.4.5 CFD of a Subsonic Jet . . . 14
2.4.6 DSMC of Flat Plate and Breakdown Surface . . . 15
2.4.7 DSMC Jet Interaction Results . . . 16
2.4.8 Other Consideration: Supersonic Jet . . . 16
2.4.9 Optimized Method . . . 16

3 Free-Molecular Regime Jet Interactions 17
3.1 Near Vacuum Nozzle Tests . . . 17
3.2 Insertion Thuster Interaction on Lunar Reconnaissance Orbiter (LRO) . . . 17
3.2.1 Computational Fluid Dynamics . . . 18
3.2.2 CFD-DSMC Interface . . . 18
3.2.3 Direct Simulation Monte Carlo . . . 19
3.2.4 Discussion . . . 19
3.3 Venting and Outgassing Contamination on an Upper Atmospheric Research Satellite (UARS) . . . 20
3.4 Attitude Control System (ACS) Plume Impingement on Solar Probe Plus . . . 20
3.5 Reaction Control System (RCS) Plume Impingment on Mir During Space Shuttle Orbiter Docking . . . 21
3.6 Summary . . . 21

4 Rarefied and Transitional Regime Jet Interactions 21
4.1 RCS Interaction Experimental Studies . . . 21
4.1.1 Centre national de la recherche scientifique (CNRS) Corner Flow Jet Interaction . . . 21
4.1.2 University of Virginia (UVA) Flat Plate Jet Interaction . . . 22
4.2 RCS Interaction Studies on the Space Shuttle Orbiter During Reentry . . . 22
4.3 RCS Interaction Studies on Japanese and European Vehicles During Reentry . . . 23

5 Planetary Probe Jet Interactions 23
5.1 RCS Interactions on Magellan During Venus Aerobraking . . . 23
5.2 RCS Interactions on Mars Global Surveyor (MGS) During Mars Aerobraking . . . 23
5.3 RCS Interactions on Phoenix During Mars Entry . . . 25
5.3.1 Trajectory Point at $Kn_L = 0.1$ . . . 26

6 Direction for Future Research 26

7 Concluding Remarks 27

References **28**

Appendix A **31**

Appendix B **32**

List of Tables

Page

1 DSMC Run Statistics for $\mathbf{T_{wall} = 100\ K}$ Lunar Reconnaissance Orbiter case on the LaRC K cluster. 33
2 DSMC Run Statistics for Solar Probe Plus on the LaRC K cluster. 33

List of Figures

Page

1 Diagram and CFD Grid for DERA RCS jet interaction experiment [15]. 33
2 CFD of DERA RCS jet interaction experiment [15]. 34
3 Bird breakdown surfaces from DERA RCS jet interaction experiment CFD solution [15]. 34
4 Setup for DSMC simulation of DERA RCS jet interaction experiment [15]. 34
5 DSMC of DERA RCS jet interaction experiment [15]. 35
6 CFD flow field of supersonic nozzle (DPLR [29]). 35
7 Schematic of Lunar Reconnaissance Orbiter (LRO) internal propulsion components. 35
8 LRO insertion thruster nozzle and external flow field CFD. 36
9 LRO insertion thruster interaction DSMC boundaries and flow field. 36
10 LRO thruster base plate heating from insertion jet interaction reverse flow. 36
11 LRO insertion thruster interaction heating and pressure loads on base plate. 37
12 DSMC of UARS with HALOE telescope optics RCS plume contamination (taken from [38]). 37
13 DSMC of Solar Probe Plus Attitude Control System (ACS) plume contamination. 37
14 Jet interaction corner flow model of Allègre and Raffin [43]. 38
15 UVA rarefied free stream RCS jet interaction experiment. 38
16 Space vehicle configurations studied internationally to assess RCS jet interaction effects. 38
17 DSMC simulation of Magellan (taken from [61]). 39
18 CFD flow field of MGS ACS thruster supersonic nozzle. 39
19 Schematic of MGS and ACS thuster continuum breakdown surface. 39
20 MGS ACS jet interaction density contours from uncoupled CFD-DSMC simulation. 40
21 Yawing moment coefficient as a function of α for MGS from ACS jet interation. 40
22 CFD of Phoenix RCS Thruster. 41
23 DSMC of Phoenix flow field at $Kn_L = 0.1$. 41
24 DSMC of Phoenix afterbody at $Kn_L = 0.1$. 41

Abstract

A numerical technique that simulates the interaction between a continuum jet and a free-molecular, rarefied or transitional flow field is presented and applied. The technique is based on selecting a boundary between the expanding jet plume and interacting flow field defined by the Bird breakdown parameter, P. By properly choosing the boundary, the jet plume computed by computational fluid dynamics (CFD) is uncoupled from the interaction region that is simulated by direct simulation Monte Carlo (DSMC). The mechanics of uncoupling the continuum and non-continuum regions is discussed first. Also, a discussion of expanding continuum plume breakdown and the formulation of the Bird breakdown parameter is presented. To show the usefulness, examples of applying the CFD-DSMC technique are given. Many of the examples were taken from projects worked by the staff of the Aerothermodynamics Branch at the NASA Langley Research Center. These examples show a variety of applications of the technique and allow those examples not previously documented to be formally presented.

Symbol List

A = area, m^2
d = diameter, m
k = Boltzmann constant, 1.3806×10^{-23} J/K
Kn = Knudsen number, λ / L
L = length, m
m = mass, kg
M = Mach number
M = molecular weight, kg/kmole
n = number density, m^{-3}
$n_\circ$ = Loschmidt's number, 2.6868×10^{25} m^{-3}
N = Avogadro's number, 6.0221×10^{26} $kmole^{-1}$
p = pressure, Pa
P = Bird breakdown parameter, $\dfrac{\vec{V} \cdot \nabla \rho}{\nu \rho} = \dfrac{1}{\nu \tau}$
q = dynamic pressure, Pa
q̇" = heat flux, W/m^2
Re = Reynolds number, $\dfrac{\rho V L}{\mu}$
$\mathbf{S_0}$ = Solar constant, 0.1366 W/cm^2
T = temperature, K
$\vec{V}$, **u** or u_i = velocity vector with components u, v, and w, m/sec
V = velocity, m/sec
V = volume, m^3
x,y,z = Cartesian coordinates, m
α = angle of attack, deg
λ = molecular mean free path, m
μ = viscosity, kg/m-sec
ν = intermolecular collision frequency, sec^{-1}
ρ = density, kg/m^3
τ = characteristic time, sec
χ_i = mole fraction of species i

Subscripts

d = characteristic diameter
eff = effective
GLL = gradient length local
jet = jet nozzle exit
l = local condition
L = characteristic length
mix = mixture
q, p = species in the mixture
$wall$ = wall
∞ = free stream

1. Introduction

Aerodynamic stability and control are critical concerns for vehicles that pass through or operate in the upper, non-continuum atmosphere for either a sustained flight profile or orbital maneuvers such as reentry, aerobraking, aerocapture, or aerogravity assist. In this portion of the atmosphere, density changes rapidly with altitude, and common aerodynamic control surfaces such as elevons, wing and body flaps, rudders, etc., are not effective. When deflected, the generated forces are small and do not adequately provide for stable flight control. Because of this, active flight control in this regime is often obtained by a reaction control system (RCS), sometimes referred to as an attitude control system (ACS). The RCS is an arrangement of jet thrusters strategically placed about the vehicle surface, offset from the center of gravity, to produce forces that generate moments to control vehicle roll, pitch, and yaw. Because the RCS ejects a continuum jet at the vehicle surface into a much lower density flow field, it is important to understand the interaction between the jet and the changing free-stream flow field to determine the local surface and global aerodynamic effects.

To quantify the effect of jet interactions, experimentation, application of the conservation laws, engineering approximations, or other numerical techniques are employed. Then information is avaliable to predict the mixing behavior and the effect of the interacting (or for freely-expanding, free-molecular, noninteracting) jets on the surrounding medium, vehicle surface, and aerodynamics. In the continuum regime ($Kn_L \lesssim 0.001$), wind tunnel experiments, engineering approximations and codes, and Computational Fluid Dynamics (CFD, see refs. [1] and [2]) are enployed to represent the flow process and jet interaction effects for specific designs. Likewise, in the free-molecular regime ($Kn_L \gtrsim 100$), jet interactions have been studied by vacuum chamber experiments, collisionless flow analysis with source-flow and line-of-sight techniques, and recently, collisionless direct simulation Monte Carlo (DSMC, see refs. [3] and [4]) simulations that describe the expanding flow and surface impingement with a measure of confidence. See, for example, Dettleff [5] and Spaid and Cassel [6], respectively, for classic reviews on the subjects. However, between the continuum and free-molecular regimes, jet interactions in the rarefied and transitional regimes ($0.001 \lesssim Kn_L \lesssim 100$) with hypersonic external flow have been studied much less. And, a fundamental knowledge of the phenomena and how best to determine its effects for specific configurations and conditions is generally not available.

2. Uncouple Continuum and Non-continuum Jet Interaction Regions

As discussed in section 1, a need exists to accurately model and understand effects of jet interactions in the rarefied and transitional, non-continuum flow regime for the next generation space vehicles, upcoming planetary exploration probes, and other vehicles that use active control because they will require RCS (or ACS) to maintain flight stability during atmospheric entry or aerobraking maneuvers. The primary purpose of this paper is to present a numerical strategy that can be applied to specific geometric problems and provide fundamental understanding of the interaction between a continuum jet and non-continuum free stream for these problems.

2.1. Jet Interaction Flow Field

A jet interacting with a rarefied or transitional flow field consists of various regimes, primarily an outer non-continuum region, an embedded inner continuum jet plume region, and an interaction zone between the two regions. A molecular simulation can be applied by a technique such as the DSMC method to the entire interacting flow field, including the continuum jet, and it will yield an accurate solution of the interacting flow field provided it is implemented correctly. However, because the jet flow begins as a high-density, continuum gas in a plenum chamber and remains in a continuum state as it expands from the nozzle exit into the lower density, non-continuum interaction region, implementation of a molecular simulation to the entire flow field is limited by current computer technology and simulation algorithms.

For example, a molecular simulation with DSMC requires a grid resolution of the order of the local mean free path, λ, which, at standard conditions, is about 7×10^{-8} m. To simulate flow at this condition in a 1 mm^3 cube with DSMC would require about 3×10^{12} cells, each with 10 simulated molecules. A typical jet interaction case may need two or more orders-of-magnitude more cells with attendant molecules–well beyond computational resources of today's supercomputers. Therefore, a solution to mixed continuum/non-continuum interacting flow requires judicious use of computational resources. For the present method, the continuum, noninteracting portion of the expanding jet flow field is computed using CFD, while DSMC is employed to determine the remainder of the interacting flow with an appropriate boundary between the two. The various methods that have been used to determine an interface between the continuum and non-continuum portions of the interacting flow field are discussed in the next section.

2.2. Continuum–Non-continuum Uncoupling Surface

A number of techniques have been developed that apply CFD and DSMC in various regions to produce mixed continuum and rarefied flow field solutions. Roveda et al. [7] discussed issues associated with coupling the continuum and rarefied

regions using uncoupled, weakly-coupled, and strongly-coupled techniques. The method developed and employed in the examples presented subsequently uncouples the jet plume from the interacting, non-continuum free stream.

This uncoupled technique is appropriate for situations where the higher density, expanding flow field is unaffected by the lower density interaction region beyond the interface; that is, information is passed only in the expanding flow direction from the high to the low density region. For the present situation, the expanding jet flow can be obtained from CFD and used as an inflow boundary condition to a DSMC simulation of the interacting, non-continuum flow field. However, to implement such an uncoupled flow solution technique, a boundary must be established between the CFD and DSMC solution domains to allow the CFD solution to capture the continuum portion of the plume that is unaffected by the interaction.

2.2.1. First Approaches

Some of the earlier approaches that were proposed and employed to numerically model and study a continuum jet interacting with a rarefied free stream are discussed in this section. CFD and DSMC were applied separately to an experiment of an axisymmetric conical configuration with an annular ring attached to the surface that simulated the jet plume as solid obstruction to the flow (Gilmore and Warburton [8]). A comparison between the numerical and experimental results showed that both the CFD and DSMC numerical results lacked a complete description of flow structures and the surface effects seen experimentally. In addition, the simulation was performed on an axisymmetric model, which is not representative of three-dimensional interactions for complex geometric configurations.

Wilmoth and Tartabini [9] and Tartabini et al. [10] took another approach applying the DSMC method to jet interaction corner flow studies. The simulation domain was populated with cells sized about twice the length of the free stream mean free path, λ_∞. The jet was approximated as a molecular inflow boundary normal to a flat plate surface. However, the jet inflow mean free path, λ_{jet}, was several orders-of-magnitude smaller than free stream mean free path ($\lambda_{jet} \ll \lambda_\infty$) resulting in an inadequate number of cells describing the higher density jet and interaction regions. Additionally, to properly model the jet interaction using this approach would require inordinate computational resources. Because an insufficient number of cells was used, flow-field gradients and local collision rates were not accurately defined. Thus, incorrect jet and interaction macroscopic properties may have influenced subsequent molecular surface collisions and led to inaccurate surface pressure, skin friction, and heating values.

Several methods exist to establish a boundary between the continuum and rarefied regimes, which have been discussed by Boyd et al. [11] and Bird [3]. Boyd et al. [11] used a gradient length local Knudsen number, $Kn_{GLL} = \lambda/L$, with the characteristic length, $L = \rho/\nabla\rho$, based on the local density gradient to determine the boundary between the continuum and rarefied regimes. The focus was primarily on flow fields with regions of compression. Their study [11] concluded that for regions with large density gradients, such as near shock waves and stagnating flows, if $Kn_{GLL} > 0.05$, the continuum approach breaks down.

2.2.2. Bird Breakdown Parameter, P

Bird [3], however, defined a continuum breakdown parameter for expanding flow. Gradients in the macroscopic flow properties are sustained by collisions between molecules. As the number of collisions decreases, these gradients cannot be maintained. The Bird breakdown parameter, P, provides a numerical variable, which is a measure of the number of molecular collisions in a characteristic time for an expanding flow. As P increases beyond a value of $P = 0.02$, the local temperature begins to depart from continuum theory because the molecular collision frequency becomes too low to provide a local equilibrium condition [3].

Because the boundary defined by Boyd et al. [11], $Kn_{GLL} = 0.05$, is based on the local density gradient for flow compression and the Bird breakdown parameter, P, is based on flow expansion [3], P is used to define the boundary between the expanding jet plume and the non-continuum, interacting flow field. Given a continuum, three-dimensional expanding flow solution from CFD, a Bird breakdown surface (see refs. [12] and [3]) can be obtained. The breakdown surface provides a natural boundary between continuum and non-continuum flow regions, and, by properly choosing the value of the surface breakdown parameter, an applicable continuum region can be determined. One difficulty is to ensure the jet plume expands outward and is not distorted by the interaction, thus allowing the jet and interaction to be uncoupled.

2.2.3. Present Technique

The approach of combining CFD and DSMC to model jet interactions was first applied to study freely expanding RCS jet plume impingement on Mir by the Space Shuttle orbiter during docking (Lumpkin et al. [13] and Rault [14]). The plume was modeled using CFD from the plenum through the nozzle into an outer region with a surrounding vacuum

boundary condition. Next, the CFD solution was analyzed to yield the Bird breakdown parameter varable, from which the $P = 0.05$ surface was extracted. Then, the DSMC plume inflow boundary was created at the breakdown surface with inflow variables interpolated from the CFD solution. Finally, DSMC was applied to obtain the simulation of the orbiter docking to Mir.

In the in-orbit docking studies, no free stream was present to interact with the expanding plume. Moreover, these studies (Lumpkin et al. [13] and Rault [14]) defined the extent of continuum flow at a plume breakdown value of 0.05. Rault [14] stated the use of this breakdown value is valid because it is based on experimental data; however, Bird [3] suggested the extent of the continuum regime for an expanding flow is at $P = 0.02$. Note that the larger the numerical value of the breakdown parameter, P, the more rarefied the plume flow field. Consequently, the breakdown parameter value given by Bird [3] provides a more conservative evaluation of the continuum regime than that of Rault [14].

This document provides a set of guidelines that defines a boundary between continuum and non-continuum regions for jet interactions in the transitional and rarefied flow regimes. By following the guidelines, numerical resources can be optimized to simulate jet interactions by employing continuum and molecular flow analyses in the regions where most appropriate. For the examples provided subsequently, a breakdown surface, $P \approx 0.02$ is employed; any variation from this value will be discussed.

2.3. Breakdown of Expanding Continuum Flow

An accurate uncoupled CFD-DSMC jet interaction solution is predicated by correctly defining a breakdown surface between the continuum and noninteracting portion of the jet plume and the interacting flow surrounding the plume. To determine the departure of an expanding flow, such as the jet, from a continuum flow condition, Bird [3] proposed that a breakdown surface be defined with an associated breakdown parameter, P, of numerical value 0.02. In this section, the theory and mechanics of producing a breakdown surface from known flow field quantities, such as those from a CFD solution, are developed and presented.

The present approach of defining the continuum breakdown of a jet plume is similar to the one first applied by Lumpkin et al. [13] and Rault [14]. The jet plume of that study was modeled using a CFD solution. The breakdown surface and the flow properties at the breakdown surface were based on the CFD solution. Outside the breakdown surface, DSMC was applied with the breakdown surface as an inflow boundary to a molecular simulation.

In the study of expanding jet flow from the Space Shuttle orbiter Primary Reaction Control System (PRCS) thrusters, Rault [14] proposed a parameter N be used to determine the boundary between the continuum and non-continuum regimes. The parameter is given as

$$\mathrm{N} = \nu\tau \tag{1}$$

where ν is the frequency of intermolecular collisions and τ is a characteristic time between collisions in the jet plume so that N is the number of intermolecular collisions in a characteristic time. Expanding the definition further, Rault [14] presents the characteristic time as

$$\tau = \frac{L}{\vec{V}} \tag{2}$$

where $\vec{V}$ is the local velocity vector and length, L, is defined as

$$L = \frac{\rho}{\nabla\rho} \tag{3}$$

and ρ is the local gas density. Therefore, substituting equations (2) and (3) into equation (1)

$$\mathrm{N} = \frac{\nu\rho}{\vec{V}\cdot\nabla\rho} \tag{4}$$

The breakdown parameter, P, of Bird [3] is just the inverse of N given by equation (4)

$$P = \frac{1}{\mathrm{N}} = \frac{\vec{V}\cdot\nabla\rho}{\nu\rho} \tag{5}$$

Using definitions for the hard sphere (HS) molecular model given by Bird in reference [3], the intermolecular collision frequency, ν, can be expressed as

$$\nu = \left(\pi \mathrm{d}^2 \mathrm{n}\right)\left(\frac{16k\mathrm{T}}{\pi \mathrm{m}}\right)^{\frac{1}{2}} \tag{6}$$

Equation (5) provides a formulation of the breakdown parameter as a function of macroscopic flow-field variables, which can be obtained from a CFD solution. Note the intermolecular collision frequency, ν, in equation (5), is defined

by equation (6), and in the definition, molecular diameter, d, molecular mass, m, temperature, T, number density, n, and the Botzmann constant, k, are required. Also, temperature dependence may be included in equation (6) by replacing the hard sphere (HS) model with a variable hard sphere (VHS) model.

For a mixture, an effective molecular diameter, $\mathrm{d}_{\mathit{eff}}$, and effective molecular mass, $\mathrm{m}_{\mathit{eff}}$, may be substituted in equation (6). A definition for the effective molecular diameter, $\mathrm{d}_{\mathit{eff}}$, is obtained by manipulating equations 1.35, 1.40, 1.41, 4.1, and 4.8 presented by Bird [3] to obtain

$$\mathrm{d}_{\mathit{eff}} = \sqrt{\frac{1}{2^{1/2}\pi \sum_{p=1}^{S}(n_p \lambda_p)}} \tag{7}$$

where S is the total number of species in the mixture and $n_p\lambda_p$ is

$$n_p\lambda_p = \frac{n/n_p}{\sum_{q=1}^{S}[(n/n_q)\pi(\frac{d_p+dq}{2})^2(1+\frac{m_p}{m_q})^{1/2}]} \tag{8}$$

Finally, an effective molecular mass, $\mathrm{m}_{\mathit{eff}}$, is given as

$$\mathrm{m}_{\mathit{eff}} = \frac{M_{mix}}{N} \tag{9}$$

Substituting the effective molecular diameter and mass obtained from equations (7) and (9), respectively, into equations (5) and (6) yields a closed set of equations to define the Bird breakdown parameter. Appendix A presents an author developed Fortran program that calculates $\mathrm{d}_{\mathit{eff}}$ using equation (7). Additionally, Appendix B presents an author written Tecplot macro-code that solves equation (5) on a CFD flow field and produces a Bird breakdown parameter field variable that can be analyzed to find the appropriate breakdown surface.

2.4. Application to Uncoupled CFD-DSMC Transitional Regime Jet Interaction

An application of a jet interaction with a near-continnum, transitional flow field is presented next; it will be shown that the value of P chosen to uncouple the continuum and non-continuum regions is sensitive to both the jet and free-stream conditions. One difficulty in defining the boundary between the two regions is to choose a Bird breakdown parameter value that assures the expanding jet does not interact with the free stream and optimizes the use of both CFD and DSMC numerical techniques, especially for non-continuum, transitional interactions.

A flat plate jet interaction is presented in this section. Glass and LeBeau [15] numerically simulated the interaction experiment that was performed by Warburton [16]. It will be shown that the experiment was conducted in the transitional regime, which is between the continuum and rarefied regimes. Because jet interactions are influenced by the flow properties of both the free stream and jet, modeling this experiment provides a unique opportunity to establish the extent of the jet interaction influence with a transitional regime free stream. Understanding gained by modeling experiments in this flow regime may extend to modeling jet interactions on flight vehicles at similar flow conditions.

2.4.1. DERA Jet Interaction Experiment

The transitional regime jet interaction was modeled based on the geometry and test conditions of one in a series of experiments in the Low Density Tunnel (LDT) at the Defence Evaluation and Research Agency (formally DERA) in Farnborough, United Kingdom by Warburton [16]. A sonic argon jet was released through a circular nozzle with an exit diameter of 0.004 m normal to the surface of a sharp-leading-edged flat plate at zero incidence. The jet, with a plenum (or total) temperature and pressure of 300 K and 34.5 kPa, respectively, was modeled to interact with a Mach 9.84 nitrogen free stream at static temperature and pressure of 65 K and 5.4 Pa, respectively. At these conditions, the free-stream mean free path, λ_∞, is about 0.2 mm with an equivalent altitude of about 60 km (COESA [17]). The Knudsen number based on the sonic jet diameter, Kn_{d}, is about 0.04, which is near the continuum limit but is still in the transitional regime.

A sketch of the flat-plate test apparatus with geometric dimensions is shown in figure 1a. The sketch locates the plate walls and the jet of the numerical model; note that a symmetry plane was placed in the center of the flat plate in the x-z plane reducing the computational domain by one half.

2.4.2. General Overview of Uncoupled CFD-DSMC Jet Interaction

Because the Knudsen number of this case is so close to that of a continuum condition, CFD was applied to the entire domain as an initial step to characterize the flow field. Once converged, the flow field solution was written in PLOT3D

format so that the data could easily be manipulated with a user written Fortran code. The solution file was post-processed to produce the Bird breakdown parameter variable. Then, a graphics visualization package was employed to evaluate the Bird breakdown surface in the jet plume region, and to determine the plume Bird breakdown parameter value, P, where the uncoupling CFD-DSMC interface should be placed.

Next, an axisymmetric CFD solution of the expanding jet was performed and analyzed, and an interface surface was defined at the appropriate breakdown parameter value. Flow property values were then interpolated from the CFD solution onto the breakdown surface, which then was used as a jet inflow boundary condition for the DSMC simulation of the transitional regime jet interaction. For this jet interaction study, the continuum jet plume portion of the flow was performed by CFD, and the molecular simulation of the jet interaction by the DSMC technique. CFD was applied by the GASP flow solver (McGrory et al. [18] and AeroSoft [19]), and the DSMC method was applied by the DSMC Analysis Code (DAC) of LeBeau [20] (also, see LeBeau [21] and Wilmoth et al. [22]). DAC is a suite of computer programs that unifies all aspects of a molecular simuation. The surface tools plus (*stp*) utility assures geometric surfaces are compatible with DAC; and DAC preprocessors (*predac* and *dpredac*), processors (*dac* and *ddac*), and post-processors (*slice* and *sprop*) setup, apply the DSMC method, and extract the simulation results, respectively. Multiprocessor and cluster preprocessing and DSMC processing are accomplised with the highly parallelized, scalable computer programs, *dpredac* and *ddac*, respectively, that are written to employ supercomputer architecture with the Message Passing Interface (MPI) communications protocol.

Sections 2.4.3-2.4.7 present a detailed discussion of the specific steps taken to produce the near continuum, transitional regime jet interaction by the uncoupled CFD-DSMC solution technique. Because this was the first use of the uncoupled method for a jet interaction in the transitional regime, the procedures presented were the ones used at that time (nearly twenty years ago) to show how they have been optimized since then.

2.4.3. CFD Jet Interaction Model

An isometric drawing showing the volume of the CFD computational domain is given in figure 1b. The domain extends 0.1 m behind the flat plate and includes the region under the plate. Effects on the upper flat plate flow from the lower plate and wake should be captured by including these regions in the computational domain. Additionally, the computational domain includes the subsonic portion of the nozzle from the plenum to the nozzle exit on the flat plate. All surfaces are modeled with a no-slip wall boundary condition, which provides for boundary layer development. The flat plate is 0.150 m long and 0.210 m wide; however, because of symmetry on the x-z plane midway of the plate, only one-half of the flow field was modeled computationally. Figure 1b shows the x-z plane of symmetry.

A GASP flow solver solution requires the inviscid and viscous flux models, chemistry, and boundary conditions be specified for the computational domain. For the present case, the inviscid flux scheme of Roe was applied to the nozzle region, and the inviscid flux scheme of van Leer was applied to all other regions. Reconstruction with flux limiting was accomplished using the method of van Albada with third-order, upwind biased accuracy. A laminar viscous flux model with all thin-layer and cross-flow terms (full Navier–Stokes approximation) was applied for the solution scheme. A second-order accurate gradient was applied to wall calculated quantities (heat flux, skin friction, etc.). Sutherland's law with Wilke's mixing model specified viscosity and conductivity transport properties. Gas chemistry was modeled as a two-species, frozen mixture in translational and rotational equilibrium. The nozzle gas was modeled as argon and the free stream gas as nitrogen. The flat plate and nozzle wall temperature was held at 300 K. All outflow boundaries were calculated as first-order extrapolated from the neighboring interior cells of the domain.

Solutions were obtained using global iterations of all regions with mesh sequencing, and convergence was based on the value of the solution L_2 norm, which provides a measure of numerical convergence by showing the root mean squared difference between flux values of two consecutive iterative steps normalized by the flux values assigned to the grid prior to starting the numerical solution. After the L_2 norm decreased to a value of about 1 x 10^{-9} based on the initial condition, the solution was assumed converged as the L_2 norm no longer decreased and the change between iterations was judged close to machine round-off error.

As a historical note, the CFD solution was accomplished on a single processor of a decommissioned Cray Y-MP supercomputer using about 44 Mbytes of RAM for the fine grid time integration and required about 60 hours to reach the L_2 norm convergence level indicated previously.

Figure 2 shows number density contour plots of the converged CFD solution. The contours are normalized by Loschmidt's number, $n_\circ$. Contours at the symmetry plane are shown in figure 2a and at the cross-flow nozzle location in figure 2b. A complex flow field is produced above the plate ($z > 0$) by the Mach 10 free stream interacting with the expanding jet. The weak, flat-plate leading-edge shock wave interacting with the strong, jet-induced shock is shown in figure 2a. The interacting flow recompresses just above and forward of the expanding jet. The recompression zone is also shown in figure 2b above the expanding jet. Also, by including the flow under the plate and wake behind the plate,

any influence of the flow about the plate on the jet is modeled.

2.4.4. *Bird Breakdown Parameter*

Employing the breakdown parameter definition developed in section 2.3, a user-written Fortran program computed the breakdown parameter field variable (eq. 5) from a PLOT3D (Walatka et al. [23]) formatted CFD solution. PLOT3D is a common file format to represent a computational grid and solution. A central differencing operator in the program calculated the density gradient term except at boundaries where a single-sided operator was used. The molecular mass and diameter of the expanding argon was used as an input to the program. The output was a PLOT3D formatted solution file containing the breakdown parameter field variable, P.

A commercially available flow visualization and analysis program, EnSight (see CEI [24]) was used to produce isosurfaces corresponding to various values of breakdown parameter, P. Isosurfaces are created with EnSight by grid cell edge interpolation to define a point value for P on the cell face. Points with the desired isovalue are connected and displayed as triangulated surface elements. An ASCII text file of a cloud of points, which spatially describes the geometry of a given P isosurface, was the output option chosen.

This technique was applied to the jet interaction PLOT3D solution file, and the results are shown in figure 3. Isosurfaces at two values of the breakdown parameter are presented in the figure. At $P = 0.01$ (fig. 3a), the surface appears as a smooth body of revolution normal to the plane of the plate surface (shown by the darker flat region in the figure) even though the breakdown parameter was calculated from a CFD solution of a complex jet interaction (see figure 2). At $P = 0.02$ (fig. 3b), however, the breakdown surface extends further from the plate surface and begins to show evidence of the free stream interaction, as indicated by the nearly diagonal jagged cut plane through the upper portion of the breakdown surface.

The irregularity of the cut plane is because the density gradient operation in equation (5) amplifies the breakdown value at the jet recompression. Effectively, when a Laplacian operation is applied to the discrete flow field values and there is a sign change in the second derivative because of the recompression, a surface feature such as the one shown on the figure can be expected. Also note that the same feature is shown in figure 3a for the $P = 0.01$ breakdown surface, except it is located away from the surface. An assessment of these results led to the choice of a value of $P = 0.01$ for the undisturbed breakdown surface for the uncoupled CFD-DSMC technique.

Based on this analysis of a near continuum, transitional regime jet interaction, several rules-of-thumb can be inferred. First, if $Kn_{\mathrm{d}} \lesssim \mathcal{O}(0.1)$, the jet interaction is in the near-continuum, transitional regime, and a CFD solution of the flow surrounding the vehicle body including the wake region with both the jet and the free stream present should be obtained prior to beginning the uncoupled technique; however, if $Kn_{\mathrm{d}} > \mathcal{O}(0.1)$, only the nozzle flow may need a CFD solution because the flow field is not near continuum. Next, the CFD solution should be closely analyzed to provide insight into the overall flow structures and specific interaction locations between the jet and free stream shock waves. Finally, the breakdown parameter field variable should be computed and analyzed to provide the P value of the undisturbed breakdown surface between the CFD and DSMC portions of the uncoupled solution and to locate any other higher density regions that may cause greater computational load by the DSMC technique.

2.4.5. *CFD of a Subsonic Jet*

Although a breakdown surface can be extracted from the overall CFD solution, for this example, an axisymmetric jet plume solution was used to create the breakdown surface. As discussed previously, by allowing the continuum portion of the higher density jet outside the nozzle exit to be determined by CFD, significant computational savings can be realized by not having to simulate that flow with DSMC. Thus, by extracting a breakdown surface at the optimal P value from a CFD solution of the jet plume, creating a compatible DSMC geometry of that surface, interpolating the plume flow properties onto the surface, and combining the resulting breakdown surface with the flat plate geometry, the two flow regimes become uncoupled. Thus, an optimized DSMC simulation of the jet interaction can be obtained.

GASP, the CFD code previously used to obtain the entire jet interaction solution discussed above, was also used to obtain an axisymmetric, freely expanding jet solution. Although the GASP solver requires a three-dimensional, finite-volume structured-grid, axisymmetric solutions were obtained by properly constructing symmetric grid planes and applying axisymmetric boundary conditions to the computational domain (McGrory et al. [18] and AeroSoft [19]).

Modeling of the axisymmetric nozzle is similar to the nozzle modeling for the interacting jet cases. That is, flow at the plenum temperature and pressure was allowed to expand through a converging nozzle to the sonic condition at the exit. However, rather than interacting with a free stream flow, the jet flow from the nozzle exit was allowed to expand further as a plume into an outer computational domain, which simulated an infinite vacuum. A first-order extrapolation from the interior was specified as the outflow boundary condition for the computational domain. Wall temperature was held constant at 300 K and a no-slip condition was applied to the nozzle and outer region walls.

One of the symmetry planes of the computational domain for the expanding axisymmetric jet is shown on the left side of figure 4a. The right side of the figure shows normalized number density contours from the CFD solution. Note that along the outflow boundary, the number density is reduced by at least four orders of magnitude from the plenum condition. The extent of the upper computational zone was chosen so that the expanding jet transitioned from continuum to rarefied flow before reaching the outflow boundary, which assured that a jet plume continuum surface could be defined within the computational domain.

2.4.6. DSMC of Flat Plate and Breakdown Surface

A noninteracting plume surface for the expanding jet is obtained from the CFD solution, which was first processed to produce a breakdown parameter PLOT3D solution file. The breakdown parameter value was chosen so that the plume did not extend into the interaction region for the free stream flow with a Knudsen number of $Kn_{\mathrm{d}} = 0.04$. Based on results from figure 3, the value of $P = 0.01$ fits this criteria. An analysis of the breakdown parameter file by the EnSight program (CEI [24]) provided the geometry of the noninteracting plume surface as a cloud of points.

Although the pointwise description given by the EnSight program correctly maps the continuum jet plume at the proper Bird breakdown parameter value, the format is not compatible as a DAC geometric surface description. The preprocessor program of DAC requires a description of all surface geometries as groups of triangulated surfaces. To create the geometry file for the present solution, the flat plate geometry and the noninteracting plume surface must be merged together in a format readable by the DAC preprocessor program.

Several software packages were required to process the geometry of the flat plate model and jet plume to produce the proper triangulated format. First, the cloud of points representing the jet plume surface was transformed to an initial graphics exchange specification (IGES) format (Smith et al. [25]), one that is common for most computer aided design (CAD) programs. A commercially available software program, Surfacer (Imageware [26]), was utilized to produce IGES-formatted surface descriptions.

To create the geometry of the flat plate model and combine it with the jet isosurface, another computer program, GridTool (Samareh [27]), was used. GridTool allows external geometric descriptions of different formats (IGES, GRIDGEN, LaWGS, PLOT3D) to be merged together with geometries created within the GridTool program. The program generates a group of surface patches with the same format that describe the entire surface geometry of interest. For the present study, the flat plate geometry, created with the GridTool program, was merged with the IGES jet plume surface obtained with the Surfacer program. A FELISA (Peirò et al. [28]) input file is generated as an output option by the GridTool program. FELISA is an unstructured finite element surface and volume grid generation program (see Peirò et al. [28] for a complete discussion of FELISA). For the present application, however, only the FELISA surface triangulation routine was used. Triangulation density of the surface is controlled by distributing sources with the GridTool program, which are read by the FELISA surface triangulation routine.

One final step was necessary to provide a compatible DAC formatted surface description for the molecular simulation. An author developed translation and boundary condition application code, *ftodac*, was applied to the FELISA output file. All surface points, the number of triangles of the surface, and triangle connectivity are rewritten from a FELISA to DAC type format by *ftodac*. Additionally, appropriate solid wall and jet plume surface boundary conditions are assigned to each triangle. All solid walls of the flat plate are treated as noncatalytic, fully diffuse surfaces with full momentum and energy accommodation. The jet plume surface is treated as an outgassing boundary with the number density, velocity, and temperature of the jet assigned to the proper boundary location. The outgassing boundary condition of the plume also assures that molecules outside the plume that are moving toward the plume surface are allowed to pass out of the DSMC domain and are removed from the simulation. Boundary conditions for the jet plume surface are interpolated from the original structured grid GASP PLOT3D solution file by a weighted distance squared subroutine of the *ftodac* program. Additionally, the plume is capped at the nozzle exit with a disk to close the geometry.

Figure 4b shows the triangulated surface description of the flat plate and jet plume surface for the argon jet interaction that was generated by the FELISA program. The figure shows the full geometry; however, for the simulation, only half of the geometry was used because of symmetry at the plate center line. The right upper corner of the figure shows a closeup view of the argon jet plume surface, which consists of 7200 triangles (of which 3600 were used because of symmetry). Note the dense surface triangulation of the surface near the jet exit. The closely spaced triangles allow a more detailed geometric and boundary condition description of the jet plume surface in the region where flow gradients are high. Also, the flat plate (to one side of the symmetry plane) was described by 25,000 triangles with over 12,000 triangles on the upper surface to produce the desired surface sampling about the jet interaction region.

2.4.7. *DSMC Jet Interaction Results*

In this section, CFD and DSMC number density contour plots are presented, compared and discussed. The contour plots use the same format to make them easier to compare (figs. 2 and 5). All of the CFD and DSMC number density flow field variables are normalized by the same value, Loschmidt's number, n_o, and presented using the same scale. Streamwise contour plots are given in figures 2a and 5a for the CFD solution and DSMC simulation, respectfully. Likewise, the cross-flow nozzle plane CFD and DSMC contour plots are given in figures 2b and 5b, respectively. Note that the nozzle and jet plume of the CFD solution are replaced by a void from the nozzle to the breakdown surface for the DSMC simulation. As discussed previously, the breakdown surface was derived from an axisymmetric CFD jet plume solution, and it represents the DSMC jet plume inflow boundary condition.

The overall contour pattern features of the CFD and DSMC flow fields resemble each other as shown by comparing figures 2 and 5, respectively. Also, both solutions yield similarly complex interaction patterns with the expanding plume. The weak shock waves produced at the sharp leading edge of the flat plate interact with the higher–pressure jet creating a strong shock wave interaction as evidenced by the number density contour plots in both of the symmetry plane (figs. 2a and 5a) and crossflow plane (figs. 2b and 5b) for CFD and DSMC figures, respectively. The DSMC simulation exhibits a stronger shock interaction because the grid was better resolved than for the CFD solution. In addition, the comparison between CFD and DSMC solutions (figs. 2 and 5, respectively) shows that the shock interaction location, structure, and strength are similar, and both techniques capture the same details below the flat plate and in the wake region aft of the plate. A more thorough comparison between the two cases is given by Glass and LeBeau [15].

2.4.8. *Other Consideration: Supersonic Jet*

The majority of jet interaction cases involve supersonic jets. Even though the method is nearly the same to produce sonic and supersonic jet CFD solutions, there is a marked difference between the plume and continuum breakdown surface shapes. Figure 4a presents the grid (on the right) and number density contours (on the left) from a sonic jet plume solution, and an inset at the upper right of figure 4b shows the $P = 0.01$ continuum breakdown surface.

Figure 6a shows a CFD solution for a supersonic jet. Note that the supersonic nozzle exit is oriented so that the flow expands from left to right (fig. 6a), and the sonic nozzle exit orientation expands the flow upward (fig. 4a). The axisymmetric solution was produced by the Data Parallel Line Relaxation (DPLR) flow solver [29] for a perfect gas (N_2). The density contours are on the lower portion of the figure, and the Bird breakdown parameter contours are on the upper portion of the figure. A comparison of the supersonic jet density contours (fig. 6a) with the sonic jet contours (fig. 4a) shows that the supersonic contours are more narrow creating isosurfaces that are longer and thinner than the ones for the sonic case. Perhaps, the difference in the density isosurfaces is because the supersonic section is contoured so that the preferred direction of the expanding gas is along the nozzle centerline, whereas for the sonic nozzle the exiting flow into a vacuum has no preferred direction. Also, note that the Bird breakdown isosurfaces are shaped similarly as the density isosurfaces; that is, the supersonic breakdown surfaces are longer and thinner than for the sonic case (compare figure 4b with figure 6a).

A final consideration is properly modeling the RCS jet chemical gas mixture. Employing the same viscous grid and flow solver (DPLR [29]), two supersonic jet solutions were produced with the difference being the chemistry model. One of them is a computation of an expanding perfect gas (N_2) (shown in figure 6a), and the other is an expanding gas mixture (NH_3–N_2–H_2), the products of a hydrazine reaction (shown in figure 6b). A comparison of the two solutions shows that the density contours of the nitrogen and hydrazine products (the lower portion of the figures) are nearly the same; however, the Bird breakdown contours of the hydrazine products (the upper portion of the figures) are much larger than those for the nitrogen. The difference may be because of the gas properties. The molecular weight of nitrogen is 28, and the molecular weight of the hydrazine reaction products is 14.7. Thus, to avoid inaccuracies in the Bird breakdown field variable and the resulant interaction simulation, it is important that care must be taken to accurately specify the RCS jet gas properties for the computational solution.

2.4.9. *Optimized Method*

The method described above to produce and uncoupled CFD-DSMC solution has been optimized for recent application. Currently, the DPLR flow solver of Wright [29] is employed to produce CFD jet plume solutions because it has the capability for chemically-reacting flows. Recently, however, Gnoffo [30] coded the FUN3D flow solver with the generic gas path chemistry model for nozzle flow problems. It is anticipated that FUN3D will soon provide unstructured grid solutions for chemically-reacting nozzle flows. No matter which CFD flow solver is used, the only requirement is that it can produce a jet plume that is simulated to exhaust into a vacuum.

After the CFD nozzle plume solution is obtained, the effective molecular properties are calculated using the method given in Appendix A. The CFD solution is post-processed using Tecplot360 [31], and within the Tecplot environment, a macro code (see Appendix B) is employed to modify the CFD solution and produce the Bird breakdown field variable, P. Bird breakdown surfaces are visualized with Tecplot, and at an appropriate value, the surface is written to a file as a cloud of points. Then, the Pointwise CFD grid generation software [32] creates a smooth triangulated surface from the surface points, which is read back into the Tecplot environment where the CFD flow field variables are interpolated and transformed into DAC in-flow boundary variables. As one of the final steps, an author written file conversion code, *tec2dac*, translates the Tecplot formatted file to DAC format. The resultant DAC compatible breakdown surface file is easily combined with the DAC surface description file, dacsd.dat, using the DAC utility program, *stp*.

3. Free-Molecular Regime Jet Interactions

The weakest interaction between a jet and the free stream occurs in the free-molecular regime. RCS thrusters maintain vehicle attitude during maneuvers such as orbital adjustments, docking, lunar orbital insertion, and manned extravehicular activities (EVA) (Dettleff [5]). Generally, jet interactions with the free stream flow are negligible on-orbit because the free stream surrounding the vehicle has many orders of magnitude fewer molecules than the high-density RCS jet flow. The RCS jet expands freely in this regime and provides thrust for vehicle control. Dettleff [5] has extensively reviewed jet plume flow for space technology applications. Although jet interactions with the free stream are not a concern, defining plume impingement effects on surrounding vehicle structural components is important. Mass, momentum, and energy are transferred from the jet plume to the surrounding vehicle structure and cause contamination, undesired forces, and structural heating. The thorough review of plume impingement by Dettleff [5] includes discussions of the effects of jet exit Reynolds number, jet plume specific heat ratio, angle and source distance of the plume surface impingement, multiple jets interacting, and correlations of these effects derived from vacuum tunnel experiments.

3.1. Near Vacuum Nozzle Tests

In 1998, the Germans compared the results of an expanding thruster plume experiment to a numerical prediction from an uncoupled CFD-DSMC technique. Details of the study were presented by Rosenhauser et al. [33]. The experimental portion of the study was performed in the Deutsches Zentrum für Lulf- und Raumfahrt (DLR) high-vacuum plume test facility, Simulationsanlage für Treibstrahlen Göttingen (STG). Plumes were produced by expanding flow from the plenum of a 0.5 N conical thruster into the high-vacuum facility. For the numerical simulation of the nozzle and plume flow, CFD was performed for the low Knudsen number, continuum portion of the flow from inside the thruster past the nozzle exit where the local Knudsen number, $Kn_{\mathrm{L}} > 0.05$. The uncoupling interface between the CFD solution and DSMC simulation was chosen at $Kn_{\mathrm{L}} = 0.05$. At the interface, information passed one-way from the CFD solution to the DSMC simulation as a boundary condition, which is appropriate for an expanding flow. Comparison between experimental and numerical results was generally good; however, Rosenhauser et al. [33] suggested that a more accurate modeling of the thruster wall temperature distribution may have decreased the difference between the experiment and simulation.

3.2. Insertion Thuster Interaction on Lunar Reconnaissance Orbiter (LRO)

A unique application of the uncoupled CFD-DSMC technique was a simulation of the Lunar Reconnaissance Orbiter (LRO) lunar insertion maneuver (Mission website [34]). It was determined during a 2006 GN&C LRO peer review that the source flow model of the insertion thrusters may not adequately show the effects of interaction between the thruster jets. Therefore, the LaRC-AB was contacted by Mr. Parker Khary of the Goddard Space Flight Center (GSFC) and asked to independently assess the insertion thruster interaction and any resultant base heating and pressure effects. To address this critical need, the uncoupled CFD-DSMC technique was applied as the independent assessment.

Four tightly-clustered insertion thrusters were to be fired simultaneously to initiate lunar orbit. The thrusters, shown in figure 7, are positioned on the vehicle as shown in the LRO schematic (fig. 7a), and a close-up view of the thruster arrangement is presented in figure 7b. An analysis of the insertion thruster interaction on the thruster base plate of the LRO was performed. The thruster base plate was modeled as a disk, and it did not include all of the structural elements and piping shown on the close-up view (fig. 7b) because those structural components were assumed not to directly affect the jet interaction. The flow field and base plate heating and pressure loads were obtained using the uncoupled CFD-DSMC solution method, are presented subsequently, and were reported to the LRO project office.

Specifically, the uncoupled CFD-DSMC method employed to predict the insertion thruster interaction proceeded as outlined below. First, CFD was applied to the gaseous mixture of hydrazine reaction products from the nozzle inflow boundary; through the subsonic chamber, the sonic throat, and diverging supersonic portions of the nozzle; out

the nozzle exit; and into a larger outer region where the gas expands into a vacuum. The outer region was sized so the expanding gas exited the region as a non-continuum outflow. Therefore, an analysis of the flow field in the outer region will yield an interface where continuum flow "breaks down" and ceases. Next, the interface surface between the continuum (CFD) and non-continuum (DSMC) portions of the flow field is extracted and employed as an inflow boundary for the DSMC simulation. The DSMC method was applied to the modeled interaction region from the interface and LRO surfaces to a noninteracting outer region. Finally, the simulation was analyzed to determine the effect of all plume-to-plume and plume-to-surface interactions either on or near the LRO surface.

This technique employs state-of-the-art numerical techniques in the regions where they are valid: CFD in the continuum thruster core region and DSMC in the non-continuum, rarefied region. Lumpkin and Larin [35] applied a similar technique to a multiplume, interacting flow field. Because of symmetry, they were able to produce a solution for the interaction by simulating one-quarter of the flow field with two adjacent, perpendicular symmetry planes. The present solution generally follows that of Lumpkin and Larin [35]; however, because of the asymmetric thruster arrangement, only one plane of symmetry could be used.

3.2.1. Computational Fluid Dynamics

An IGES file locating the four insertion thrusters, support brackets, and base was obtained from GSFC. In addition to locating the structural elements, the IGES file also provided the internal surface geometry of the insertion thrusters, which was used as a template for the CFD grid. Figure 8a shows the axisymmetric grid that was built from the IGES file for the internal portion of the thruster to the external flow field. Note that the thruster is modeled with a converging, then diverging section, so the flow is expanded from the chamber to a sonic condition at the throat, to supersonic flow before being released out of the nozzle exit. The axisymmetric grid was used to produce a typical thruster CFD solution, which is translated and rotated to the appropriate 3-D thruster position and boundary. For this project, the General Aerodynamics Simulation Program (GASP) of AeroSoft, Inc. was employed to yield the CFD solution (see refs. [36] and [37]).

Four species were simulated: nitrogen (N_2), hydrogen (H_2), ammonia (NH_3), and water (H_2O). The product mole fractions were obtained assuming a feed pressure of 1.59 MPa, which extrapolated to a mixture with 67 percent ammonia dissociation yielding mole fractions, χ_i, for N_2, H_2, NH_3, and H_2O of 0.30, 0.52, 0.17, and 0.01, respectively. Additionally, the chamber gas temperature and pressure were 1130 K and 0.717 MPa, respectively. Because the static temperature drops quickly from the chamber, through the nozzle, and out to the simulated vacuum, the mixture was treated as frozen.

CFD was performed using GASPv4.2 with a third-order, upwind-biased Roe scheme and a modified ENO limiter. The flow was treated as laminar, and it was computed employing grid sequencing with coarse, medium, and fine grid cells during which the residual dropped to machine zero (about 18 orders of magnitude). Flow field density contours that resulted from the CFD are shown in figure 8b. Note that the flow direction is from left to right as depicted by the arrow in the figure. Also, the flow proceeds from the high-density thruster chamber (shown as red) into the low-density vacuum region (shown as blue).

3.2.2. CFD-DSMC Interface

An interface between the continuum and non-continuum regions of the flow was created from the CFD solution, and those details are presented next. The first step was to determine the effective diameter and molecular weight variables from the flow field solution. These variables were calculated using the Fortran code presented in Appendix A. Then, the effective diameter, molecular weight, and other CFD flow field field variables (see figure 8b) were post-processed with the Tecplot macro-code presented in Appendix B. Finally, the Bird breakdown parameter, P, is calculated by the macro-code and easily visualized within the Tecplot environment. Depending on the value of P, the flow field (fig. 8b) was separated into two regions, one containing the continuum flow field of the thruster plume and the other region, the non-continuum portion of the plume. Generally, for an expanding flow field, a value of the breakdown parameter in the range from $0.02 \leq P \leq 0.05$ represents the location where continuum flow breaks down and non-continuum begins. For this simulation, the value of $P = 0.02$ was intially chosen to define the breakdown surface. However, when analyzed, the interface surfaces of the four clustered thrusters overlapped. Therefore, to avoid the overlap, the interface surface was reshaped to allow the DSMC to simulate flow interactions between the thrusters. The reshaped interface surface that was produced is presented in figure 9a. Note that for this configuration there is a symmetry plane at $x = 0$ with two symmetric breakdown surfaces on the symmetry plane.

3.2.3. *Direct Simulation Monte Carlo*

The DSMC method for the LRO was applied by the DSMC Analysis Code (DAC) of LeBeau [20]. The multiprocessor DAC programs, *dpredac* and *ddac*, were used for this application and are written to employ supercomputer architecture with the Message Passing Interface (MPI) communications protocol. The code was compiled with OpenMPI and executed on the LaRC K cluster, a center resource that provides mid-range computing cabability. At that time, the LaRC K cluster consisted of an SGI ICE Altix 8200 and an SGI Network Attached Storage (NAS) device with dual-socket, quad-core, 2.66 GHz Intel 5355 (2 x 4MB cache), 1333MHz FSB compute CPUs interconnected by a 4X DDR Infiniband (about 16 Gbit/sec). Run statistics for the $\mathrm{T_{wall}} = 100$ K case are given in table 1. The simulation took nearly 46 hours to complete, and the final adaptation cycle employed 1.2 billion simulated molecules distributed on 511 compute processors.

DAC uses a Cartesian grid for the flow field simulation that is clipped by triangulated geometry elements such as those shown in figure 9a. Flow properties on the thruster CFD-DSMC interface surface were extracted from the CFD flow solution, specifically the *u*-, *v*-, and *w*-velocity components, number density, species mole fraction, and static temperature. The simulation sampling began after the number of molecules became steady and continued until a significant number of samples were acquired so that the flow field and surface properties did not change further.

3.2.4. *Discussion*

Three wall temperature cases were produced using the uncoupled CFD-DSMC technique. Wall temperatures of 100, 300, and 500 K were chosen to bracket the expected extremes. In addition, the variation of wall temperature allows for the effect of wall temperature change to be quantified. In particular, the wall temperature effect on heat transfer can be assessed and, if needed, accounted for in a heat transfer analysis.

The symmetry plane flow field produced by the uncoupled CFD-DSMC technique is shown in figure 9b. Note that the flow field from the thrusters compresses between them, and a portion of it is redirected and impinges on the base. The redirected flow impingement causes mass contamination, an adverse thrust increment, and energy transfer from the high-enthalpy thruster flow on to the surface. For the hydrazine thruster, mass contamination may be from one or more of the four species: nitrogen, hydrogen, ammonia, and water.

Next, to quantify base heating, normalized heat transfer contours are presented in figures 10a, 10b, and 10c for wall temperatures of 100, 300, and 500 K, respectively. LRO heating results are normalized by the solar constant, $\mathbf{S_0}$. For all three wall temperature cases, the greatest heating is confined to the region between the four thrusters. Outside this region, the heating quickly falls off to the background level. The maximum heating is nearly 6.5 times the solar constant for a wall temperature of 100 K (see figures 10a and 11a). As the wall temperature increases to 500 K, the maximum heating decreases to 4 times the solar constant. Interestingly, surface heating in this rarefied environment is similar to continuum jet impingement heating where the heating rate is proportional to the heat transfer coefficient times the temperature difference–as the wall temperature increases, the driving potential (or temperature difference) decreases, thus, decreasing the surface heating.

Figure 11b shows a pressure contour plot typical of the three temperature cases. Note that the pressure contour plot is similar to those presented previously for heating in figure 10 because of redirected thruster flow impingement. The maximum pressure on the base plate between the thrusters is 14.6 Pa. When integrated over the represented base region, the adverse thrust increment is 0.6 N. Because of this relatively low value, the maximum pressure and the adverse thrust increment posed no significant problem.

Because the unique application of the method to closely clustered thrusters had not been previously documented, a complete discussion of the local interaction flow field and surface heating and pressure is presented. The flow field and subsequent base plate heating was obtained using the uncoupled CFD-DSMC solution method, and the method identified flow compression between the insertion thruster plumes on the LRO. The flow compression redirects thruster flow onto the base surface between the thrusters (fig. 9b), which allows mass, momentum, and energy impingement on the base. The effect of mass contamination is minimal if the surface is compatible with thruster reaction products nitrogen, hydrogen, ammonia, and water. In addition, reverse thrust is small as the integrated surface pressure on the base is only 0.6 N. However, maximum base surface heating occurs when the wall temperature is 100 K, and it is nearly 6.5 times the solar constant. At 500 K, the maximum heating decreases to about 4 times the solar constant. The higher heating region is localized between the thrusters and dissipates quickly outside the region.

Experience has shown the solution technique employed provides a conservative estimate for the reversed thruster flow impinging on the base. To further refine the non-continuum solution, DSMC including the plumbing, support structure of the thrusters, and curved base region geometry are required. The greater grid definition would require more computational resources and time than that used for the present analysis. However, this may not provide a better

solution because the reversed thruster flow impingement is localized in a region between the thrusters without geometric details (see figure 7b).

3.3. Venting and Outgassing Contamination on an Upper Atmospheric Research Satellite (UARS)

Not only are RCS thrusters a source of gas impingement for vehicles in orbit, but venting and outgassing from the vehicle surface pose a contamination threat to optical surfaces. Rault and Woronowicz [38] and Woronowicz and Rault [39] applied the DSMC method to analyze surface contamination on the Upper Atmospheric Research Satellite (UARS) halogen occultation experiment (HALOE) telescope optics from surface outgassing, equipment venting, and attitude thruster firing while in orbit. The USRS is represented by the surface grid of figure 12a. Note that the HALOE instrument is depicted in the inset.

For the simulation, molecules from surface sources were introduced into the DSMC domain as either emitting gases with no bulk velocity or as drifting Maxwellian free jets from the surface. The study provided simulations of the local contamination field and surface contamination on the UARS HALOE instruments, which showed that estimates based on engineering codes were too conservative. Results for heavy outgassed molecules ($M = 100$) are shown in figure 12b.

These results were documented in 1995, and the technique used represented the state-of-the-art at that time. Rault developed the DSMC code used in this study [40] from one Bird earlier had developed [41] by enhancing the fine grid region to better represent the near-vehicle flow field. The technique split the computational space into a coarse grid and a near-vehicle fine grid with the simulation for each grid on a different processor. Thus, the code was optimized for two single processor desktop workstations. The near-vehicle, interdomain consisted of 35,000 cells with 330,000 simulated molecules, and the outer domain consisted of 7500 cells with 400,000 simulated molecules. It took nearly 200 CPU hours for the simulation to complete, which was run simultaneously on two Spark 2 workstations (see Woronowicz and Rault [39]).

This study also showed that DSMC techniques and computational resources were improving, and more accurate DSMC calculations of the local flow field and surface contamination about geometrically complex satellites in orbit could be performed with turnaround times of just over a week on desktop workstations (Rault and Woronowicz [38]). A major deficiency with the method presented by Rault and Woronowicz [14] and [38], however, is that accuracy in the continuum flow region adjacent to the outgassing surface or thruster plume was limited because the DSMC technique required excessive computational resources to provide a complete representation of the flow field in those regimes not avaliable on the two workstations.

3.4. Attitude Control System (ACS) Plume Impingement on Solar Probe Plus

In 2010, Dr. Mary Kae Lockwood of the Johns Hopkins University Applied Physics Lab (APL) requested the LaRC-AB perform ACS thruster firing simulations of the Solar Probe Plus to determine the extent of surface contamination for those conditions. The Solar Probe Plus mission is to understand how the Sun's corona is heated and solar wind is accelerated. (See APL [42] for a thorough discussion of Solar Probe Plus.) Attitude control for the vehicle is provided by hydrazine ACS thrusters, and surface contamination is a major concern because surface-mounted instrumentation may be compromised by the presence of the three modeled hydrazine reaction products: nitrogen (N_2), hydrogen (H_2), and ammonia (NH_3).

For these simulations, the thruster vendor provided a continuum flow field solution of the hydrazine reaction products exiting from the nozzle into a vacuum. The flow field solution was analyzed yielding a Bird breakdown surface based on the criteria $P = 0.02$. The breakdown surface was incorporated into the vehicle geometry, the DSMC method applied, and the simulation results were provided to the APL science team, who then factored the results into the final spacecraft design.

One of the DSMC simulations with thrusters RL-1 and RL-2 firing is shown in figure 13. Figure 13a is a flow field slice at the RL-1 thruster location, and figure 13b is a flow field slice at the RL-2 thruster location. Results for this case show that the RL-1 thruster plume impinges on the solar panel backside and scatters as shown in figure 13a. Because of flow scattering, a portion of the thruster flow field is redirected onto the surface resulting in contamination shown in figure 13c.

For this case, the DSMC method was applied by the DAC code of LeBeau [20] on the LaRC K cluster; similarly, it was applied to the Lunar Reconnaissance Orbiter (section 3.2). That is, the code was compiled with OpenMPI and executed on dual-socket, quad-core, 2.66 GHz Intel 5355 (2 x 4MB cache), 1333MHz FSB CPUs. As shown in table 2, the simulation took just over 26.5 hours on the LaRC K cluster. The final adaption employed 150 million simulated molecules distributed into 15 million cells, with an average of 10 molecules per cell.

It is important to note the DSMC technology state-of-the-art change between 1995 and 2010, which can be seen by comparing the turnaround time and problem size of the UARS contamination simulation presented in section 3.3 with

the present Solar Probe Plus DAC contamination simulation. In 1995, a 750,000 simulated molecule simulation took nearly 200 CPU hours on two workstations, and in 2010, the present simulation was over 7.5 times faster using 256 CPUs with nearly 200 times the number of simulated molecules.

3.5. Reaction Control System (RCS) Plume Impingment on Mir During Space Shuttle Orbiter Docking

Lumpkin et al. [13] and Rault [14] studied plume impingement from the Space Shuttle Orbiter RCS during docking maneuvers with the Russian space station Mir to ensure jet plume impingement did not damage the Mir solar panels or cause attitude control problems with a CFD-DSMC approach. Prior to the CFD-DSMC approach, plume impingement effects would be quantified by engineering codes making use of corrections such as those presented by Dettleff [5]; however, the Shuttle Orbiter docking maneuver with the Mir was simulated by a combined CFD-DSMC approach to provide an independent assessment of pressure and heat loads. The CFD solution technique was applied to the expanding plume flow in the immediate vicinity outside of the RCS nozzle exit, and a continuum breakdown boundary, the Bird breakdown surface [3], was obtained from the CFD solution of the expanding plume. A breakdown surface defined the outer extent of the RCS plume continuum flow region where the Navier-Stokes equations were applied. Flow properties from the CFD solution at the breakdown surface location were then used as an inflow boundary for a molecular simulation applied by the DSMC technique. This uncoupled CFD-DSMC approach of Lumpkin et al. [13] and Rault [14] provided high-fidelity estimates for pressure and heat loads on the Mir space station from close proximity Shuttle Orbiter RCS engine firing during docking maneuvers.

3.6. Summary

RCS impingement and surface outgassing studies such as those described above show the usefulness of the DSMC technique in analyzing flow about vehicles in-orbit in the free-molecular flow regime. The DSMC technique has almost become a necessary tool for the spacecraft designer in determining contamination, pressure, and heat loads for space vehicles in-orbit. Although engineering codes that predict contamination fields about satellites with line-of-sight view factors using approximations such as those given by Dettleff [5] provide a first-order estimate of the effects of the plume impingement contamination, DSMC molecular simulations provide a more accurate estimate of the contamination flow field. Intermolecular collisions and multiple surface interactions are modeled directly with DSMC, as opposed to the ad hoc models for the return flux used in engineering codes. In addition, a comparison between the DSMC applied to the UARS in 1995 and the Solar Probe Plus in 2010 provides a reference point as to the state-of-the-art change over a 15-year period. The comparison shows simulation wall-clock time was over 7.5 times faster using 256 CPUs with nearly 200 times the number of simulated molecules.

4. Rarefied and Transitional Regime Jet Interactions

4.1. RCS Interaction Experimental Studies

In addition to studies of configuration-specific RCS jet interactions in the free-molecular flow regime described in section 3, some experimental and accompanying computational studies of rarefied and transitional flow interacting with continuum jets have been accomplished. These studies were performed to increase fundamental understanding of the flow physics and resultant surface effects from jet interaction with a rarefied free stream flow on simple shapes. The experiments also provide a database to validate existing and developing computational techniques, which can then be applied to obtain jet flow field interactions for the more complex flight configurations and flight conditions.

4.1.1. Centre national de la recherche scientifique (CNRS) Corner Flow Jet Interaction

A French experiment performed in the SR3 wind tunnel of the Centre National de la Recherche Scientifique (CNRS) in Meudon, France (Allègre and Raffin [43] and Allègre et al. [44]) models a jet interaction in a corner to simulate effects such as those caused by an RCS jet near a wing-fuselage juncture. The model used in the experiment is shown in figure 14.

Two sharp leading edge flat plates oriented perpendicular to each other form a corner. The horizontal plate had an orifice oriented normal to its surface through which a supersonic jet is injected. Both plates, at zero incidence to a rarefied Mach 20 N_2 free stream, were instrumented with pressure orifices. Surface pressure distributions and surface oil flow visualizations at various free stream and jet flow conditions from the experiment were presented by Allègre and Raffin [43].

Wilmoth and Tartabini [9] and Tartabini et al. [10] applied the DSMC technique to the French corner flow jet interaction experiment. For the simulation, the jet flow at the nozzle exit was “modeled as a circular disk contained

within the horizontal surface across which molecules are injected by sampling from a streaming Maxwellian distribution" (Wilmoth and Tartabini [9]). Molecules were ejected from the surface with an average velocity and temperature based on calculated nozzle exit conditions. Results of the DSMC study showed the simulation produced higher jet induced wall pressure than was measured during the experiment. A similar modeling of jet flow was chosen by Rault et al. [45], Shane et al. [46], and Shane [47] for the DSMC simulation of both the Magellan and Mars Global Surveyor during actively controlled planetary aerobraking maneuvers. If the jet plume flow near the nozzle is in a continuum state, application of the DSMC technique to the near nozzle exit flow is not appropriate. Instead, a mixed solution methodology, which captures the continuum flow by a CFD solution and the rarefied flow by a DSMC simulation, would yield the proper flow field solution.

4.1.2. University of Virginia (UVA) Flat Plate Jet Interaction

Staack et al. [48] investigated the interaction between a continuum transverse jet and a hypersonic rarefied free stream flow at the UVA hypersonic facility. For this project, a planar laser-induced iodine fluorescence (PLIIF) measurement technique was extended to measure temperatures down to 5 K at pressures from 1 Pa to 50 kPa by including the nuclear hyperfine structure of iodine into a previous fluorescence model. The PLIIF technique measured temperature, pressure, and velocity for two cases: first, the free jet test section of the wind tunnel , and, second, an RCS flow field consisting of a flat plate with transverse jet. The first data set validated the PLIIF technique by comparisons with known relations for a free jet and to provide extensive data on the free jet test section. A hypersonic wind tunnel and an optical measurement technique were developed and provided experimental measurements necessary to validate the computational model. The RCS measurements represent the first experimental data set of their kind and are avaiable to validate the CFD-DSMC technique. A sketch of the RCS model and the experimental velocity contours from the PLIIF measurement technique are shown in figure 15.

4.2. RCS Interaction Studies on the Space Shuttle Orbiter During Reentry

The Space Shuttle orbiter was a manned, winged spacecraft that employed RCS from entry interface through the rarefied regime into the continuum regime until the aerodynamic control surfaces became effective and allowed the vehicle to maneuver during its terminal glide to a downrange runway landing. Roll control jets were operated up to a flight dynamic pressure of 480 Pa, and pitch control jets to a dynamic pressure of 960 Pa [49]. However, the aft yaw RCS jets were required for trim from entry interface with the atmosphere down to flight speeds of about a Mach number of one (Kanipe [49] and Romere et al. [50]).

During the first Shuttle orbiter entry, discrepancies between flight and predicted aerodynamics were observed from the transitional to the continuum regime flight Mach number of about 10. During this hypersonic portion of reentry, RCS was employed extensively for orbiter control; however, only marginal control was available from the flight control system because the underlying aerodynamic database was developed from conventional wind tunnel scaling parameters.

Pitching moment based on body flap deflection was incorrectly predicted (Throckmorton [51]), and induced rolling moment from aft RCS yaw jet interaction was overpredicted (Kanipe and Roberts [52], Romere et al. [50], Allègre et al. [43], and Scallion [53]). Rarefaction and high-temperature effects during high Mach number orbiter flight were much different from those scaled wind tunnel results, which may have led to the incorrect extrapolation (Allègre et al. [43]). Scallion [53] suggested the most probable cause of the discrepancy was that vehicle wake correlations were not included in the scaling parameters. Even though discrepancies existed between predictions and flight, the uncertainty bounds of the flight control system during the first Shuttle orbiter flight was wide enough to account for the differences (Kanipe [49] and Romere et al. [50]) without a catastrophic accident.

Although the Space Shuttle orbiter was operational for three decades with a vehicle flight control system based, first on extrapolated wind tunnel scaling parameters, then modified as flight operational data became available, NASA proved by the success of the program that aerodynamic control of a winged, space vehicle was maintainable during descent from orbit to landing. The gross effect of the RCS jet interaction on vehicle control was obtained by flight experience, but local flow field and surface effects caused by the interaction were not well understood (Scallion [53]). By better understanding the effects of RCS jet interactions, especially in the rarefied high-speed flight regime, the uncertainty in force and moment predictions may have been reduced resulting in increased flight control efficiency (Romere et al. [50]). Thus, for similarly configured vehicles, the RCS jet interaction lessons learned from the Shuttle orbiter are available and should be closely reviewed when applicable.

Defining the effects of RCS interactions in the rarefied flight regime poses unique challenges for vehicle design and aerodynamic control. As discussed in section 4.2, the Shuttle orbiter flight control laws used wind tunnel derived scaling parameters. Because numerical techniques at that time were considered unreliable, extensive RCS interaction wind tunnel tests were required. As confidence in numerical techniques has grown, different approaches have evolved

and have been used to define the effects of RCS interactions. Given below are examples that show the maturation of numerically defining these jet interactions.

4.3. RCS Interaction Studies on Japanese and European Vehicles During Reentry

During the 1990s, much international interest was generated in defining jet interaction effects for then planned space vehicles after reentry. The H-II Orbiting Plane (HOPE), shown in figure 16a, was envisioned to be an unmanned Japanese reusable space transportation vehicle. The vehicle was designed to use RCS for control in the rarefied regime after deorbit (Yamamoto [54] and Nagai et al. [55]). Flight tests to verify CFD and experimental scaling parameters were accomplished by the Japanese Hypersonic Flight Experiment (HYFLEX) (Watanabe and Takaki [56] and Watanabe et al. [57]). Analysis of flight data from HYFLEX was planned to aid in developing the HOPE control laws (Watanabe et al. [57]). The method employed by the Japanese to define the effects of RCS interactions for the HOPE space vehicle was to develop scaling parameters based on a mix of CFD solutions, wind tunnel tests, and flight experiments.

In addition, the European Space Agency (ESA) was interested in defining the effects of RCS interactions for their HERMES spacecraft shown in figure 16b. Pörtner [58] reviewed the Shuttle orbiter RCS scaling parameters used for predicting aerodynamic flight performance, made recommendations for HERMES RCS wind tunnel tests (Pörtner [58]), and tested the HERMES 1.0 configuration in the German DLR V2G hypersonic vacuum tunnel to assess RCS interaction effects on the thruster leading edge (Pörtner [59]). Although the HOPE (Kallender [60]) and the HERMES programs were cut, early jet interaction studies showed the importance placed on an RCS interaction database for these vehicles.

5. Planetary Probe Jet Interactions

Another vehicle class, planetary probes, such as the Magellan and Mars Global Surveyor (MGS), used an RCS/ACS in a rarefied atmosphere during the actively controlled aerobraking phase of their missions; for example, see Rault [61], Rault et al. [45], Shane et al. [46], and Shane [47]. In this section, three planetary probes, which used actively controlled RCS jets, and were studied by the LaRC-AB are presented. First, the Venus Magellan probe is discussed; then RCS predictions for the Mars Global Surveyor are presented and discussed; and finally, RCS interactions on the Phoenix probe, which delivered the Curiosity rover to Mars, are presented.

5.1. RCS Interactions on Magellan During Venus Aerobraking

Rault [61] studied an actively controlled aerobraking maneuver of the Magellan spacecraft in the atmosphere of Venus using the Direct Simulation Monte Carlo method. After the primary surface mapping mission objectives were met, interest focused on obtaining higher resolution atmospheric planetary measurements, which required the spacecraft to be placed into a lower Venus orbit. Rault [61] used a DSMC molecular simulation to analyze aerodynamic characteristics of Magellan during flight through the rarefied atmosphere. For one of the final experiments of Magellan in 1993, the Windmill Experiment, RCS was used to offset torque induced by the solar panels pinwheeling while the spacecraft traveled about the lower orbit.

One goal of the experiment was to obtain an indirect measurement of solar panel and vehicle surface momentum accommodation in the Venus atmosphere (Rault et al. [45]). Large discrepancies existed between flight data and aerodynamic moments predicted by a free molecular analysis. Application of the DSMC method by Rault et al. [45], in which the RCS jets were modeled as a source flow from the vehicle surface, showed better agreement with the flight data. The much higher density RCS jet plumes interacted with the free stream and shadowed the solar panels and a portion of the spacecraft from the lower density incoming flow, thus affecting vehicle aerodynamic loads. Figure 17a shows the Magellan reference frame and the location of the high gain antenna, engine compartment, payload bay, and solar panels with respect to the probe main bus. The interacting flow field is shown in figure 17b. Figure 17 was taken from reference [61], and the free stream density contour plot is of poor quality.

5.2. RCS Interactions on Mars Global Surveyor (MGS) During Mars Aerobraking

A planetary exploration program was established, and the MGS was the first spacecraft of a planned series of orbiters and landers of the Mars Surveyor Program (NASA [62] and Goldin [63]). A pair of spacecraft were planned to be sent to Mars every 26 months for the next 5 years after the MGS. The next surveyor mission was to be the Mars Surveyor 1998, but it was renamed Mars Climate Orbiter. It was to be actively controlled by RCS during aerobraking to circularize the orbit about Mars. Launched December 11, 1998, the Mars Climate Orbiter disintegrated during orbital insertion September 23, 1999 because incorrectly programmed thruster output instructions were uploaded into the probe's computer before reaching Mars.

The first Mars orbiter of the program, the MGS, was designed to obtain surface, atmospheric, and magnetic data about the planet while in orbit with its onboard instrumentation. The mission life was planned to end early January 2000. Launched on November 7, 1996, the MGS reached Mars orbital insertion September 11, 1997. The original mission plan called for an aggressive series of about 300 aerobraking orbits where the vehicle would lose orbital momentum to frictional drag by successively passing the vehicle, in an aerobraking configuration, through the upper Mars atmosphere during periapsis (the lowest altitude of an orbit). The purpose of the aerobraking activity was to passively change the highly elliptic post-insertion orbit to a more circular mapping orbit without extensive expenditure of onboard propellant. Lee [64] provides a comprehensive explanation of the aerobraking maneuver and other aspects of the MGS mission.

The original aerobraking schedule and configuration were changed because the solar panel yoke, which connects the two-axis gimbal mechanism to the solar panel array, was damaged when the MGS solar panels were deployed shortly after launch. However, the original aerobraking configuration was extensively studied by Shane [47] and Shane et al. [46] using the DSMC code, X2, of Rault [14] and [61]. Shane's aerobraking studies included simulations of the attitude control system thrusters during periapsis when the atmospheric density of an orbit is greatest and jet interaction with the free stream has the most affect. Because the study included ACS jet interaction cases and was thoroughly documented, some of the ACS jet interaction cases were chosen to compare with results produced by the uncoupled CFD-DSMC technique. Two solutions for each angle of attack were made, one flow field with no jet interaction and the other, a jet interacting with the flow field. Also, note that the ACS thruster of X2 jet interaction study (refs. [47] and [46]) was modeled as a disc with continuum jet nozzle exit conditions imposed as an inflow of molecules into the DSMC simulation.

Mars atmospheric conditions for the jet interaction studies of Shane [47] were density, ρ_∞ = 12 x 10^{-6} kg/m^3, temperature, T_∞ = 148 K, and velocity, V_∞ = 4811 m/s. Also, the free stream gas volumetric composition was 95.5% CO_2, 2.7% N_2, 1.6% Ar, and 0.2% O_2. Based on these conditions and the jet exit diameter of 0.015 m, the Knudsen number, Kn_d = 49, which describes a jet interaction with a moderately rarefied flow. Therefore, because the MGS ACS jet interacted with a rarefied free stream, a conserative Bird breakdown value of P = 0.02 was chosen to define the jet breakdown surface.

An axisymmetric CFD solution for the ACS thruster was obtained from the GASP flow solver [19] on the computational domain shown in figure 18a. Thruster plenum conditions were T = 1167 K and p = 978 kPa, and the hydrazine reaction products were modeled as frozen with volumetric compositions of 0.19% ammonia, 30% nitrogen, and 51% hydrogen imposed at the plenum plane. The nozzle wall boundary condition was no-slip at a constant temperature of 500 K. From the plenum, the gas mixture expanded through a converging-diverging nozzle (see figure 18a) and exited the nozzle into a region simulating a vacuum.

Outside the nozzle, the flow expansion region was bounded by a slip wall, which extended 45° from the nozzle centerline axis (Morris [65]). The outer bounding angle was chosen for the expansion region to prevent the CFD solution from diverging if the local temperature became artificially negative during the solution process, which may occur for larger turning angles.

The flow field of the ACS thruster outside the nozzle shown in the figure was analyzed to determine the extent of continuum flow. As with the other jet interaction cases, the Bird breakdown parameter, P, defined by equation (5) with the collision frequency, ν, defined by equation (6), provides a consistent method to determine the location of continuum flow breakdown. The chosen breakdown surface at P = 0.02 is shown in figure 18b as the red line.

The original aerobraking configuration of the MGS, shown in figure 19a, provides the directional orientation of the MGS during an aerobraking pass. The upper right hand side of the figure presents a 3-D axis, which shows the MGS model coordinate directions. Note that the solar panels are configured so that they are swept back 30° from the x-y plane during the aerobrake maneuver to provide a nominally stable aerodynamic shape.

The main bus of the MGS has dimensions of about 1.5 m square in the x-y plane and is about 3 m high in the z-direction, and the solar panel array, including the drag flap at the end of the panel, is about 5 m in length and 2 m wide. Figure 19a also shows the location of one of four rocket engine modules, which consists of three ACS thrusters (two facing forward and one sideways for roll control). The other three modules are located symmetrically about the main bus in the same x-y plane. Lee [64] discusses these and other MGS details in greater depth.

Figure 19b shows a close-up view of the P = 0.02 Bird breakdown surface. The surface was created by rotating the red colored line in figure 18b about the x-axis to make a solid geometry. The solid geometry was triangulated, had the CFD flow properties interpolated onto it, written in DAC format, and correctly oriented and combined with the MGS geometry. Ultimately, DSMC for the uncoupled CFD-DSMC simulations was performed on the triangulated geometry depicted in figure 19.

Because these were some of the first LaRC-AB jet interaction cases performed by DAC (circa 1997), the parallel version, *ddac*, was employed on branch desktop SGI workstations with R10000 CPUs over the local network when they were not used during the night and weekends. The total time to produce a molecular simulation for the $\alpha = 0°$ case was

222.6 node hours, and the final adapted grid solution required 332 Mbytes of distributed memory. The second adapted grid consisted of about 310,000 active cells with 3.17 million simulated molecules. Once the number of molecules in the simulation became steady, the sampling arrays were cleared, and 2500 steady state samples were obtained so that the statistical error of the simulation is about two percent. Computational time and memory requirements for the other angle-of-attack cases were similar. Today's supercomputers would produce solutions for these cases at least two orders-of-magnitude quicker; however, at that time, the simulations were state-of-the-art.

Flow field density contours from the uncoupled CFD-DSMC simulation of the Mars Global Surveyor ACS jet interactions are shown in figure 20. At $\alpha = -15°$ (fig. 20a), the plume begins as a symmetrical shape; however, further from the jet exit, the free stream flow turns the jet plume outboard because the plume momentum is overcome by the free stream. The same behavior is exhibited for the case at $\alpha = 15°$ (fig. 20b), except the free stream flow turns the jet plume toward the spacecraft main bus because the flow direction, as depicted in the figure, is from the left lower corner to the right upper corner, rather than from the right lower corner to the left upper corner as shown in figure 20a.

The post-processing routine of the DAC, *sprop*, was employed to calculate aerodynamic moments from the MGS molecular simulations. The point about which moments were taken is the same location used previously by Shane [47], which is at the center of the MGS main bus in the x-y plane and at the z-location near the attachment of the solar panel yoke and main bus. To obtain the yawing moment coefficient, C_{Mx}, the moment was normalized by the product of the reference area, $A = 17.5$ m^2, the reference length, $L = 9$ m, and the free stream dynamic pressure, $q = 1.39$ Pa. Calculated yawing moment coefficients for the MGS as a function of angle-of-attack about the x-axis, which is oriented in the direction shown by the 3-D axis in the upper right side of figure 19a, are presented in figure 21.

The square symbols shown in the figure are from the study by Shane [47], and the circular symbols are from the uncoupled CFD-DSMC technique. Open symbols represent no jet interaction cases, and closed symbols represent those cases with ACS jet interaction. Additionally, the direct thrust contribution of the ACS jet is included in all of the C_{Mx} jet interaction results presented in the figure. ACS thrust was calculated from the previously discussed axisymmetric CFD results. Although Shane [47] did not include the direct thrust contribution in his study, the X2 jet interaction results have been modified to include the direct thrust contribution. The single ACS jet thrust contribution to the yawing moment coefficient is $C_{Mx,jet} = -0.014$, thus, the effect of including jet thrust to the aerodynamic moment coefficient is to bias the data represented by the solid symbols in figure 21 to an equilibrium trim condition of $\alpha \approx 1.5°$ ($C_{Mx} = 0$).

Several conclusions can be made concerning the $C_{Mx} = f(\alpha)$ curve shown in figure 21. The consequence of the ACS jet on the moment coefficient is not a superposition of the thrust contribution with the no ACS jet moment coefficient curve. Thruster plume shadowing of various portions of the MGS surface as a function of angle-of-attack alters the surface pressure distribution, which, when integrated over the surface, changes the slope of the C_{Mx} vs. α curve (to a larger negative value) for the aerobraking MGS configuration as well as shifting the trim attitude by 1.5°.

Moreover, for particular angle-of-attack ranges, the jet affects C_{Mx} differently because the net effect of direct thrust and plume shadowing varies with α. Thrust reversal occurs for $\alpha < 4.5°$; that is, the negative moment increment from the ACS jet contribution does not cancel the positive moment generated from the redistribution of surface pressure because of the thruster plume shadowing on the MGS surface. At $\alpha \approx 4.5°$, the ACS jet thruster has no net effect on the C_{Mx} value when compared to the no jet C_{Mx} value. However, for $\alpha > 4.5°$, the change in C_{Mx} from the no jet value is negative; that is, the shadowing effect of the ACS jet on the moment is in the same direction as the direct thrust moment; therefore, only for $\alpha > 4.5°$ is the ACS jet thruster providing a contribution in the expected direction.

The comparison presented in figure 21 for the MGS jet interaction cases (solid symbols) shows that predictions from the present uncoupled CFD-DSMC method are in good agreement with those of Shane [47] for the ACS jet interacting with a moderately rarefied flow. Good agreement between the two independent studies gives increased confidence in both results. Additionally, these studies provide insight into the underlying flow physics of the interaction, which is needed by mission planners to determine the effect of a jet thruster interacting with a rarefied flow field for the particular configuration and mission being studied.

5.3. RCS Interactions on Phoenix During Mars Entry

As a final example in this section, the uncoupled CFD-DSMC technique was exercised to predict the aerodynamic effects of the interaction between an RCS jet and the external rarefied flow field during the actively controlled Mars atmospheric entry of the Phoenix capsule. Dyakonov, et al. [66] investigated and reported on the interaction throughout the entry trajectory in the rarefied, transitional, hypersonic, and supersonic flight regimes. Results of the analysis at hypersonic and supersonic conditions suggested there was significant change in the vehicle aerodynamics because of RCS interference with the local flow, which reduced the effect of the thrusters, and may produce control reversal. However, very little interference was predicted in rarefied and transitional regimes, and some of those results at $Kn_L = 0.1$ are presented next. Therefore, a recommendation was made to the project office to widen the deadbands on

the controller system to minimize RCS thruster use through the hypersonic and supersonic flight regimes, where RCS performance would be uncertain [66].

5.3.1. *Trajectory Point at* $Kn_L = 0.1$

An analysis at a rarefied flow condition ($Kn_L = 0.1$) was performed to determine if there is an interaction between the thruster and free stream. Because the flow field contains both a high pressure thruster, which expands into a rarefied external flow, when applying the uncoupled CFD-DSMC technique, the flow is split into two regions: the continuum region from the thruster plenum to the continuum breakdown surface and the rarefied region outside the continuum flow that captures the interaction. CFD was applied to the continuum region using the GASP flow solver [37]. GASP provided stable CFD iterations when producing the solution from the chamber to the expanding flow outside the RCS thruster. The three-dimensional flow solution was performed on a 19-block, 3.14 million cell grid. Inflow gas to the thruster chamber was modeled as partially dissociated, catalyzed hydrazine.

For the CFD, the back shell wall was treated as a slip boundary, and the outflow boundary was a vacuum. A slice through the three-dimensional continuum solution at the center of the nozzle is shown in figure 22a. Note that the outer boundary of the CFD solution extends beyond the continuum regime so it can be analyzed to find locations where flow breakdown occurs. As discussed previously, the Bird breakdown field variable was extracted from the flow field. For the thruster plume, that location is identified by a constant value of the Bird breakdown parameter, $P = 0.02$, which is shown as the red line in figure 22a. Also, figure 22b shows the back shell of Phoenix, two orthogonal plane cuts through the plume CFD solution (one in the x-plane, and the other in the z-plane), and the extracted continuum breakdown surface.

The next step to determine the aerodynamic changes caused by the RCS thruster firing is to provide a DSMC simulation of the rarefied flow field with and without the thruster firing. A triangulated geometry of the Phoenix outer mold lines and thruster continuum breakdown surface was created for the simulation. Flow properties were interpolated from the CFD solution and assigned to the appropriate surface triangles on the breakdown surface to create the thruster inflow boundary for the DSMC simulation.

Finally, the DAC code [20] was employed to produce the DSMC simulated rarefied flow fields. Two simulations were conducted at these conditions: one without the RCS thruster firing, as a baseline, and the other with the thruster firing to compare with the baseline. The flow fields for the two simulations are shown in figure 23. Comparing figures 23a (no RCS) and 23b (with RCS), the downstream wake density increases significantly with the thruster firing. However, the flow field at $Kn_L = 0.1$ for either case shows no sign of recirculation, which would cause the high density thruster flow to impinge directly on the afterbody and produce regions of high pressure to alter vehicle aerodynamics.

Figures 24a and 24b show corresponding afterbody surface pressure contours for the no thruster and with RCS thruster cases, respectively. As discussed above, since no recirculation was detected in the flow field, the surface pressure only increased locally near the jet exit because of the proximity of the thruster. Also, because the forebody pressure for the configuration was much greater than the afterbody pressure, even with the thruster firing, the vehicle aerodynamics was not greatly affected by the jet interaction in the rarefied regime.

6. Direction for Future Research

To more fully examine the interaction of continuum jets with rarefied flow, additional experimental and numerical studies are needed. Suggestions for some of these studies are itemized below:

- As a further validation of the present uncoupled CFD-DSMC technique, for example, a comparison between results from the current transitional-rarefied simulation and the experiment, when available, is needed.
- Systematic studies of jet interactions from the near-continuum, transitional to the rarefied flow regime using generic models, such as a flat plate at nonzero ($\pm\alpha$) incidence, cones, hemisphere-cones, corners, rear-facing steps, etc., which may represent local vehicle surfaces that issue reaction control jets, are needed to fill a database of the resultant jet interactions as a function of Kn_d.
- As shown previously, the molecular weight of the RCS gas greatly affects the extent of the Bird breakdown parameter (see the comparison in figure 6). Hence, jet interaction studies are needed to determine the effect of jet molecular weight as a function of Kn_d.
- Jet interaction studies in the near-continuum, transitional regime will allow a better understanding of the Bird breakdown parameter value to assure the surface is an outflow where the uncoupled CFD-DSMC technique can be applied similar to the first example discussed in section 2.4.

- The RCS nozzle exit on the surface of a transatmospheric vehicle is blended to the outer mold line and does not necessarily issue normal from the surface. To understand this "real life" situation, studies of curved, scarfed exit, non-normal issuing jet interactions are needed.
- Studies to define the effect of clustered multiple jets on the interaction are needed. Generally, RCS jets are arranged so they are either fired singly or, if more thrust is needed, in groups of more than one. Multiple jet interaction studies will provide insight into how best to model the continuum portion of the flow to apply a numerical CFD-DSMC uncoupled scheme.
- Next generation DSMC codes that can better simulate continuum flow conditions so that the numerical solution of continuum jets interacting with rarefied to near-continuum free stream flow fields would not require the CFD step of the uncoupled CFD-DSMC technique.

7. Concluding Remarks

An uncoupled CFD-DSMC technique has been developed and applied to experiments, flight vehicles, and in-orbit satellites. It provides solutions for RCS/ACS jet interactions in the near-continuum, transitional regime to those in the rarefied flow regime. Because the density for these jet interactions spans many orders of magnitude, the technique is applied to two regions: one of a jet as it expands through the nozzle and outside the nozzle as a freely expanding plume using CFD and the other region where the interaction between the jet and the free stream occurs using the DSMC method. For both flow regions, the continuum and molecular analyses are uncoupled at an appropriate Bird (or continuum) breakdown surface.

Uncoupling the continuum and non-continuum portions of an interacting flow at an appropriate jet plume surface offers computational advantages because continuum CFD does not apply everywhere in the flow field and performing simulations exclusively with DSMC would require huge computational resources. It is estimated that the CFD-DSMC technique can reduce DSMC requirements for the entire flow field solution of jet interaction problems by about six orders of magnitude for a sonic jet interaction and about three orders of magnitude for a highly-expanded supersonic jet interaction.

The uncoupled CFD-DSMC technique was applied to examples from $Kn_{\mathrm{d}} = 0.04$ to on-orbit, rarefied regime cases where $Kn_{\mathrm{d}} > 100$. It was shown for the lowest Knudsen number, near-continuum, transitional regime case that care must be taken to choose the appropriate Bird breakdown parameter value so that the high density jet plume can be uncoupled from the DSMC simulation. For other jet interactions, which are in the transitional to more rarefied flow regime, application of the method with a $P = 0.02$ plume provides a reasonable surface to uncouple the continuum jet from the surrounding interaction with the rarefied flow.

The uncoupled technique was also applied to an aerobraking flight condition of the Mars Global Surveyor spacecraft with an attitude control system jet interaction in the rarefied regime corresponding to $Kn_{\mathrm{d}} = 49$. Results of the present method compared well with previously published results from the X2 DSMC code, which gives credence to applying the present method to non-continuum jet interactions.

References

[1] Anderson, Jr., J.D. *Computational Fluid Dynamics*. McGraw-Hill Higher Education, New York, 1st edition, 1995.

[2] Pletcher, R.H., Tannehill, J.C. and Anderson, D.A. *Computational Fluid Mechanics and Heat Transfer*. CRC Press Taylor & Francis Group, Boca Raton, FL, third edition, 2013.

[3] Bird, G.A. *Molecular Gas Dynamics and the Direct Simulation of Gas Flows*. Clarendon Press, Oxford, 1994.

[4] Bird, G.A. *The DSMC Method*. CreateSpace an Amazon company, Seattle, WA, version 1.1 edition, 2013.

[5] Dettleff, G. Plume flow and impingement in space technology. *Prog. Aerospace Sci.*, 28:1–71., 1991. Pregamon Press, Great Britain, 1991.

[6] Spaid, F.W. and Cassel, L.A. Aerodynamic interference induced by reaction controls. AGARDograph No. 173 (ADARD-AG-173), Advisory Group for Aerospace Research and Development, December 1973.

[7] Roveda, R., Goldstein, D.B. and Varghese, P.L. A combined discrete velocity/particle based numerical approach for continuum/rarefied flows. AIAA Paper 97–1006, American Institute of Aeronautics and Astronautics, January 1997.

[8] Gilmore, M.R. and Warburton, K. Axi-symmetric hypersonic jet interaction: A combined experimental and computational study II. AIAA Paper 95–0414, American Institute of Aeronautics and Astronautics, January 1995.

[9] Wilmoth, R.G. and Tartabini, P.V. Three-dimensional DSMC calculations of jet/corner flow interactions. In *Proceedings of the 19th International Symposium on Rarefied Gas Dynamics*, Oxford University, Oxford, England, July 1994.

[10] Tartabini, P.V., Wilmoth, R.G. and Rault, D.F.G. Direct simulation Monte Carlo calculation of a jet interaction experiment. *Journal of Spacecraft and Rockets*, 32(1):75–83, Jan–Feb 1995.

[11] Boyd, I.D., Chen, G. and Candler, G.V. Predicting failure of the continuum fluid equations in transitional hypersonic flows. *Physics of Fluids*, 7(1):210–219, January 1995.

[12] Bird, G.A. *Molecular Gas Dynamics*. Clarendon Press, Oxford, 1976.

[13] Lumpkin III, F.E., LeBeau, G.J. and Stuart, P.C. A CFD/DSMC analysis of plumes and plume impingement during Shuttle/Mir docking. AIAA Paper 95–2034, American Institute of Aeronautics and Astronautics, June 1995.

[14] Rault, D.F.G. Methodology for thruster plume simulation and impingement effects characterized using DSMC. AIAA Paper 95–2032, American Institute of Aeronautics and Astronautics, June 1995.

[15] Glass, C.E. and LeBeau, G.J. Numerical study of a continuum sonic jet interacting with a rarefied flow. AIAA Paper 97–2536, American Institute of Aeronautics and Astronautics, June 1997.

[16] Warburton, K. Defence Evaluation and Research Agency, personal communication, 1997.

[17] COESA. *U. S. Standard Atmosphere, 1976*. NOAA, NASA, USAF, Washington, D.C., October 1976.

[18] McGrory, W.D., Slack, D.C. and Applebaum, M.P. and Walters, R.W. *GASP Version 2.2, The General Aerodynamic Simulation Program*. AeroSoft, Inc., 1993.

[19] AeroSoft. *GASP Version 3, The General Aerodynamic Simulation Program, Computational Flow Analysis Software for the Scientist and Engineer, User's Manual*. AeroSoft, Inc., May 1996.

[20] LeBeau, G.J. and Lumkin III, F.E. Application highlights of the dsmc analysis code (dac) software for simulating rarefied flows. *Computer Methods in Applied Mechanics and Engineering*, 191(6–7):595–609, 2001.

[21] LeBeau, G.J. A parallel implementation of the direct simulation Monte Carlo method. *Computer Methods in Applied Mechanics and Engineering, Parallel Computational Methods for Flow Simulation and Modeling*, 174:319–337, 1999.

[22] Wilmoth, R.G., LeBeau, G.J. and Carlson, A.B. DSMC grid methodologies for computing low-density, hypersonic flows about reusable launch vehicles. AIAA Paper 96–1812, American Institute of Aeronautics and Astronautics, June 1996.

[23] Walatka, P.P., Buning, P.G., Pierce, L. and Elson, P.A. PLOT3D user's manual. Technical Memorandum 101067, NASA, March 1990.

[24] CEI. *EnSight User Manual for Version 5.5.2*. Computational Engineering International, Inc., Research Triangle Park, North Carolina, 1996.

[25] Smith, B., Rinaudot, G.R., Reed, K.A. and Wright, T. Initial Graphics Exchange Specification (IGES), version 4. NBSIR report 88–3813, National Bureau of Standards, Warrendale, PA, June 1988.

[26] Imageware. *Surfacer User's Guide*. Imageware, Inc., Ann Arbor, Michigan, 1995. SUR.UG./4-95.

[27] Samareh, J. Gridtool: A surface modeling and grid generation tool. In *Proceedings of the Workshop on Surface Modeling, Grid Generation, and Related Issues in CFD Solutions*, pages 821–831. NASA, May 1995. NASA CP–3291.

[28] Peirò, J., Peraire, J. and Morgan, K. FELISA SYSTEM, Version 1.1, Reference Manual, Part 2–User Manual. Swansea technical report, University College of Swansea, Swansea, U. K., August 1994.

[29] Wright, M.J. and Mangini, N. *Data Parallel Line Relaxation (DPLR) Code Zion - Version 4.02.2 User Manual*. NASA, 2011.

[30] Nielsen, E.J., Biedron, R.T., Park, M.A., Hammond, D.P., Gnoffo, P.A., Carlson, J-R., Thomas, J.L., Lee-Rausch, E.M., White, J.A., Carpenter, M.H., Jones, W.T., Rumsey, C.L., Vatsa, V.N., Derlag, J.M., Wood, W.A., Kleb, B., O'Brien Jr., D.M., Smith, M.J. and Lynch, C.E. Fun3d–analysis & design. http://fun3d.larc.nasa.gov. Accessed: Sep 11, 2013.

[31] Tecplot, Inc. Tecplot 360. http://www.tecplot.com/. Accessed: Aug 19, 2013.

[32] Pointwise, Inc. Pointwise. http://www.pointwise.com/pw/. Accessed: Aug 19, 2013.

[33] Rosenhauer, M., Plähn, K. and Hannemann, K. Comparison of Decoupled Hybrid Navier–Stokes — DSMC Calculations with Experiments in Plumes. In *21th International Symposium on Rarefied Gas Dynamics, Book of Abstracts, Volume 1, Oral Sessions*, Universite de Provence, Marseille, France, July 1998. July 1998.

[34] NASA. Lunar reconnaissance orbiter. http://www.nasa.gov/mission_pages/LRO/main/index.html#.UeVwsrZ8zTU. Accessed: Jul 16, 2013.

[35] Lumpkin III, F.E. and Larin, M.E. Simulation of the plume from the firing of four R4D engines on the H-2 transfer vehicle using GASP and DAC codes. JANNAF paper, Joint Army Navy NASA Air Force Interagency Propulsion Committee, June 2006.

[36] Walters, R.W., Cinnella P. and Slack, D.C. A status report on GASP: A general aerodynamic simulation program. NASP Paper Paper Number 9, The National Aerospace Plane (NASP) Program, 1989.

[37] AeroSoft. *GASP Version 4.0 User's Manual*. AeroSoft, Inc., 2002. ISBN 09652780-5-0.

[38] Rault, D.F.G. and Woronowicz, M.S. Application of Direct Simulation Monte Carlo to satellite contamination studies. *Journal of Spacecraft and Rockets*, 32(3):392–397, May–Jun 1995.

[39] Woronowicz, M.S. and Rault, D.F.G. On predicting contamination levels of haloe optics aboard uars using direct simulation monte carlo. AIAA Paper 93–2869, American Institute of Aeronautics and Astronautics, July 1993.

[40] Rault, D.F.G. Aerodynamics of the shuttle orbiter at high altitudes. *Journal of Spacecraft and Rockets*, 31(6):944–952, Nov–Dec 1994.

[41] Bird, G.A. Application of the direct simulation monte carlo method to the full shuttle geometry. AIAA Paper 90–1962, American Institute of Aeronautics and Astronautics, June 1990.

[42] Johns Hopkins University Applied Physics Laboratory (APL). Solar probe plus–a nasa mission to touch the sun. http://solarprobe.jhuapl.edu/. Accessed: Jul 9, 2013.

[43] Allègre, J. and Raffin, M. Experimental study on control jet interaction (final report), ESA/ESTEC contract 111 191. Technical Report 608/91.1043, CNRS Aerothermique RC-91-11, SESSIA, December 1991.

[44] Allègre, J., Raffin, M. and Caressa, J.P. Experimental investigation of transverse jet effects related to hypersonic space vehicles. In Battrick [67], pages 165–170. ESA-SP-318.

[45] Rault, D.F.G., Cestero, F.J. and Shane, R.W. Spacecraft aerodynamics during aerobraking maneuver in planetary atmospheres. AIAA Paper 96–1890, American Institute of Aeronautics and Astronautics, June 1996.

[46] Shane, R.W., Rault, D.F.G. and Tolson, R.H. Mars Global Surveyor aerodynamics for maneuvers in Martian atmosphere. AIAA Paper 97–2509, American Institute of Aeronautics and Astronautics, June 1997.

[47] Shane, R.W. Aerothermodynamics of the Mars Global Surveyor spacecraft. Master's thesis, George Washington University, Washington, DC, December 1997.

[48] Staack, D., McDaniel, J.C., Glass, C.E. and Miller, C. Experimental study of interacting rarefied and continuum flow. AIAA Paper 2001–2762, American Institute of Aeronautics and Astronautics, June 2001.

[49] Kanipe, D.B. Plume/flowfield jet interaction effects on the space shuttle orbiter. *Journal of Spacecraft and Rockets*, 20(4):351–355, Jul-Aug 1983.

[50] Romere, P.O., Kanipe, D.B. and Young, J.C. Space shuttle entry aerodynamic comparisons of flight 1 with preflight predictions. *Journal of Spacecraft and Rockets*, 20(1):15–21, Jan–Feb 1983.

[51] Throckmorton, D. Today's technology for tomorrow's launch vehicles. *Aerospace America*, 33(6):20–24, June 1995.

[52] Kanipe, D.B. and Roberts, B.B. Evolution of the wind tunnel test program for space shuttle orbiter jet interaction upon entry and comparison of predictions with flight test results. In *Proceedings of the JANNAF 13th Plume Technology Meeting*, pages 83–94, April 1982. CPIA Publication 357.

[53] Scallion, W.I. Space shuttle reaction control system - flowfield interactions during entry. In David A. Throckmorton, editor, *Proceedings of the Orbital Experiments (OEX) Aerothermodyamics Symposium*, pages 345–370, Williamsburg, Virginia, April 1995. NASA. NASA Conference Publication 3248.

[54] Yamamoto, Y. Numerical simulation of hypersonic viscous flow for the design of H-II Orbiting Plane (HOPE) Part II. AIAA Paper 91–1390, American Institute of Aeronautics and Astronautics, June 1991.

[55] Nagai, S., Hozmi, K., Yoshizawa, A., Hara, N., Fujii, K., Bito, H. and Katurahara, T. Hypersonic wind tunnel tests of RCS jet interference. In *Proceedings of the Nineteenth International Symposium on Space Technology and Science*, pages 423–430, Yokohama, Japan, 1994.

[56] Watanabe, S. and Takaki, R. RCS gas-jet interaction experiment. In *Proceedings of the HYFLEX/HOPE-Symposium*, pages 130–137, July 1996.

[57] Watanabe, S., Takaki, R. and Yamamoto, Y. RCS gas-jet interactions in the hypersonic flight experiment, HYFLEX. AIAA Paper 97–0524, American Institute of Aeronautics and Astronautics, January 1997.

[58] Pörtner, Th. Simulation requirements for RCS plume-flowfield interaction modelling on a winged reentry vehicle. In Battrick [67], pages 101–106. ESA-SP-318.

[59] Pörtner, Th. First experimental assessment of RCS plume-flow field interaction on Hermes leading edge thruster configuration. In *Computational and Experimental Assessment of Jets in a Cross Flow*, pages 31–1–31–13, Winchester, United Kingdom, April 1993. AGARD Conference Proceedings 534.

[60] Kallender, P. Japan cuts spending; HOPE killed. *Space News*, 8(29):1,19, July 21-27 1997.

[61] Rault, D.F.G. Aerodynamic characteristics of the Magellan spacecraft in the Venus upper atmosphere. *Journal of Spacecraft and Rockets*, 31(4):537–542, Jul–Aug 1994.

[62] NASA. *1996 Mars Missions, Press Kit*. National Aeronautics and Space Administration, November 1996.

[63] Goldin, D.S. *NASA Strategic Plan*. National Aeronautics and Space Administration, Washington, D. C., February 1996.

[64] Lee, W. Mars Global Surveyor project mission plan document, final version, rev. B, MGS 542–405. JPL D–12088, JPL–NASA, November 1996.

[65] Morris, J. Primex Aerospace Corporation (formally Rocket Research Company), personal communication, 1998.

[66] Dyakonov, A.A., Glass, C.E., Desai, P.N. and Van Norman, J.W. Analysis of effectiveness of Phoenix entry reaction control system. *Journal of Spacecraft and Rockets*, 48(5):746–755, September–October 2011.

[67] B. Battrick, editor. *Aerothermodynamics for Space Vehicles, Proceedings of the First European Symposium*, ESTEC, Noordwijk, The Netherlands, May 1991. ESA-SP-318.

[68] WIKIPEDIA. Hope-x. http://en.wikipedia.org/wiki/HOPE-X. Accessed: Jun 25, 2013.

[69] WIKIPEDIA. Hermes (spacecraft). https://en.wikipedia.org/wiki/Hermes_(spacecraft). Accessed: Jun 25, 2013.

Appendix A: Fortran program to determine effective molecular gas mixture properties

```
      program diameter
c
c     Compute effective diameter and molecular weight for a gas mixture
c     of O2, N2, O, N, Ar, CO2, H2, H, He, CH4, and H20 based on the
c     definition of mean free path. See eqns. 1.35, 1.40, 1.41, 4.1,
c     4.8, 4.45, and 4.55 in "Molecular Gas Dynamics and the Direct
c     Simulation of Gas Flows" by GA Bird
c
      implicit real*8 (a-h,o-z)
      real*8 none,mmix
      real*8 xm(11),dm(11),mw(11),mm(11),nlam(11)
      data dm/3.9600e-10,4.0700e-10,3.0000e-10,3.0000e-10,4.1700e-10,
     &        3.8969e-10,2.5010e-10,2.4542e-10,2.3300e-10,3.9666e-10,
     &        6.6350e-10/
      data mw/31.9988,28.0134,15.9994,14.0067,39.9480,
     &        44.0098,2.01588,1.00794,4.002602,16.04246,
     &        18.0160/
      nspec=11
      none=-1.000
      one=1.000
      u=1.660539e-27
      two=2.000
      zero=0.000
      pi=acos(none)
c
      do ispec=1,nspec
      mm(ispec)=mw(ispec)*u
      enddo
c
c     enter the mole fraction of each species (#-species)
c     1-O2 2-N2 3-O 4-N 5-Ar 6-CO2 7-H2 8-H 9-He 10-CH4 11-H20
c
      xm(1) =0.0
      xm(2) =0.0
      xm(3) =0.01
      xm(4) =0.01
      xm(5) =0.0
      xm(6) =0.0
      xm(7) =0.0
      xm(8) =0.01
      xm(9) =0.0
      xm(10)=0.0
      xm(11)=0.97
c
c     calculate the effective diameter and molecular weight
c
      do ip=1,nspec
      if(xm(ip).lt.1.e-20)xm(ip)=1.0e-20
      denom=zero
            do iq=1,nspec
            term1=xm(iq)*pi
            term2=((dm(ip)+dm(iq))/two)*((dm(ip)+dm(iq))/two)
            term3=sqrt(one+(mm(ip)/mm(iq)))
            denom=denom+term1*term2*term3
            enddo
      nlam(ip)=xm(ip)/denom
      enddo
      sumnlam=zero
      do ip=1,nspec
      sumnlam=sumnlam+nlam(ip)
      enddo
      deff=sqrt(one/(sqrt(two)*pi*sumnlam))
      mmix=zero
      do i=1,nspec
      mmix=mmix+xm(i)*mw(i)
      enddo
      write(*,100)deff
      write(*,200)mmix
100   format(1x,'mixture effective diameter, d = ',es9.3,' m')
200   format(1x,'mixture molecular weight, M = ',f6.3,' kg/kmole')
      stop
      end
```

Appendix B: Tecplot macro-code to determine Bird breakdown parameter, P

```
#!MC 1400
# Created by Tecplot 360 build 14.0.0.25211
$!VarSet |MFBD| = './'
#
# declare constants
#
# k    : Boltzmann constant, 1.380649e-23 J/K
# A    : Avogadro's number, 6.022141e26 1/kmole
#
$!VarSet |k| = 1.380649e-23
$!VarSet |A| = 6.022141e26
#
# input variables
#
# determine d and M of the mixture from FORTRAN program in Appendix A
# and enter values below
#
# d    : molecular diameter, m
# M    : molecular weight, kg/kmole
#
$!VarSet |d| = 4.337e-10
$!VarSet |M| = 14.59
#
# input variables (format of CFD file)
#
# x    (v1): Cartesian x-coordinate, m
# y    (v2): Cartesian y-coordinate, m
# z    (v3): Cartesian z-coordinate, m
# rho  (v4): density, kg/m**3
# u    (v5): u-velocity, m/sec
# v    (v6): v-velocity, m/sec
# w    (v7): w-velocity, m/sec
# T    (v8): temperature, K
#
# output variables
#
# nu   (v9): frequency of intermolecular collisions
# tau (v10): characteristic time between collisions
# P   (v11): Bird breakdown parameter
#
$!RENAMEDATASETVAR
  VAR = 1
  NAME = 'x, m'
$!RENAMEDATASETVAR
  VAR = 2
  NAME = 'y, m'
$!RENAMEDATASETVAR
  VAR = 3
  NAME = 'z, m'
$!RENAMEDATASETVAR
  VAR = 4
  NAME = '<greek>r</greek>, kg/m<sup>3</sup>'
$!RENAMEDATASETVAR
  VAR = 5
  NAME = 'u, m/sec'
$!RENAMEDATASETVAR
  VAR = 6
  NAME = 'v, m/sec'
$!RENAMEDATASETVAR
  VAR = 7
  NAME = 'w, m/sec'
$!RENAMEDATASETVAR
  VAR = 8
  NAME = 'T, K'
$!ALTERDATA
  EQUATION = '{<greek>n</greek>, sec<sup>-1</sup>}=(PI*|d|*|d|*v4*|A|/|M|)*sqrt(16.*|k|*v8/PI/(|M|/|A|))'
$!ALTERDATA
  EQUATION = '{<greek>t</greek>, sec}=abs(v5*ddx(v4)+v6*ddy(v4)+v7*ddz(v4))/1/v4'
$!ALTERDATA
  EQUATION = '{<times><b><i>P</i></b></times>}=abs(v5*ddx(v4)+v6*ddy(v4)+v7*ddz(v4))/v9/v4'
$!RemoveVar |MFBD|
$!RemoveVar |k|
$!RemoveVar |A|
$!RemoveVar |d|
$!RemoveVar |M|
```

Table 1. DSMC Run Statistics for $T_{wall} = 100$ K Lunar Reconnaissance Orbiter case on the LaRC K cluster.

Grid Sequence	Simulated Molecules	Samples	CPUs	Run time, hrs.
Uniform	94.2 million	1250	128	13.8
1^{st} Adaptation	170.7 million	2500	128	1.8
2^{nd} Adaptation	255.9 million	12500	256	10.4
3^{rd} Adaptation	1.2 billion	5000	512	19.9

Table 2. DSMC Run Statistics for Solar Probe Plus on the LaRC K cluster.

Grid Sequence	Simulated Molecules	Samples	CPUs	Run time, hrs.
Uniform	1.6 million	750	128	0.22
1^{st} Adaptation	43.5 million	10000	128	3.44
2^{nd} Adaptation	110.7 million	10000	128	6.35
3^{rd} Adaptation	147.0 million	10000	256	14.60

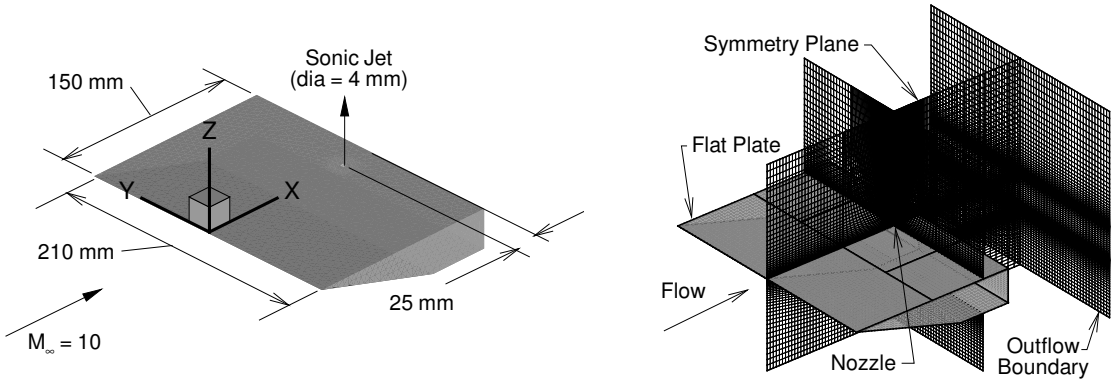

a) Surface geometry and boundary conditions. **b) Flow field grid and boundary conditions.**

Figure 1. Diagram and CFD Grid for DERA RCS jet interaction experiment [15].

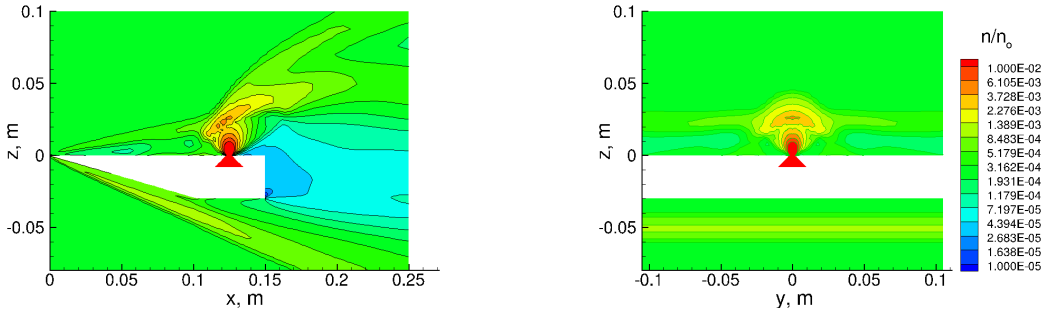

a) Flow-field symmetry plane number density contours. **b) Flow-field cross-flow plane number density contours at nozzle.**

Figure 2. CFD of DERA RCS jet interaction experiment [15].

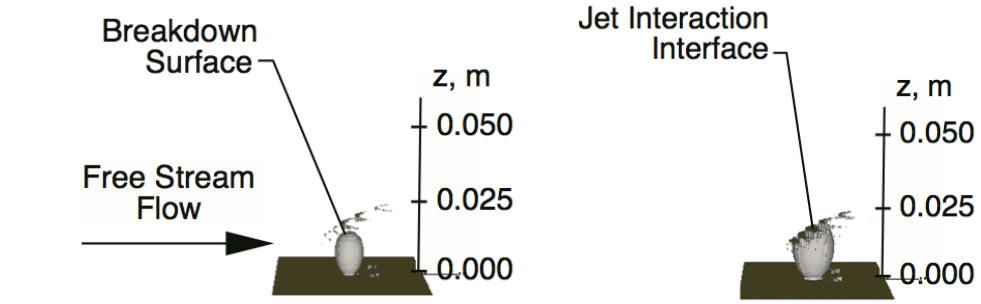

a) P = 0.01. **b) P = 0.02.**

Figure 3. Bird breakdown surfaces from DERA RCS jet interaction experiment CFD solution [15].

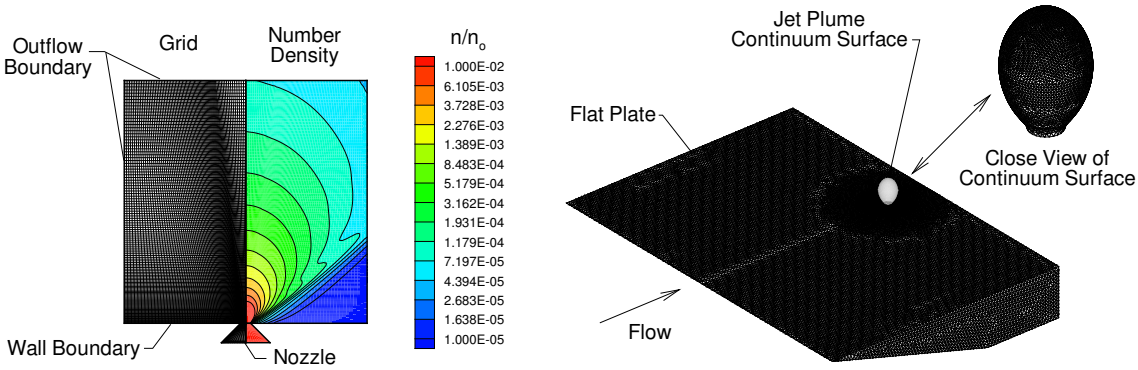

a) Expanding jet grid and number density contours. **b) Flat plate and jet continuum surface geometries.**

Figure 4. Setup for DSMC simulation of DERA RCS jet interaction experiment [15].

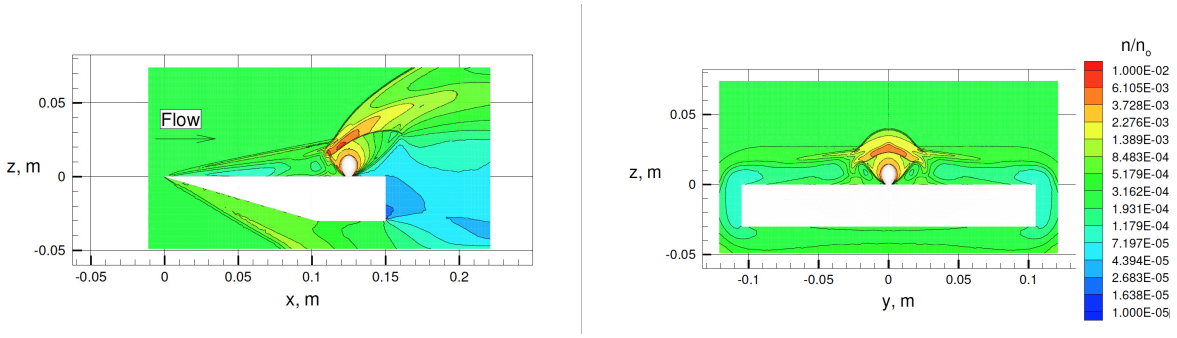

a) Flow-field symmetry plane number density contours.

b) Flow-field cross-flow plane number density contours at nozzle.

Figure 5. DSMC of DERA RCS jet interaction experiment [15].

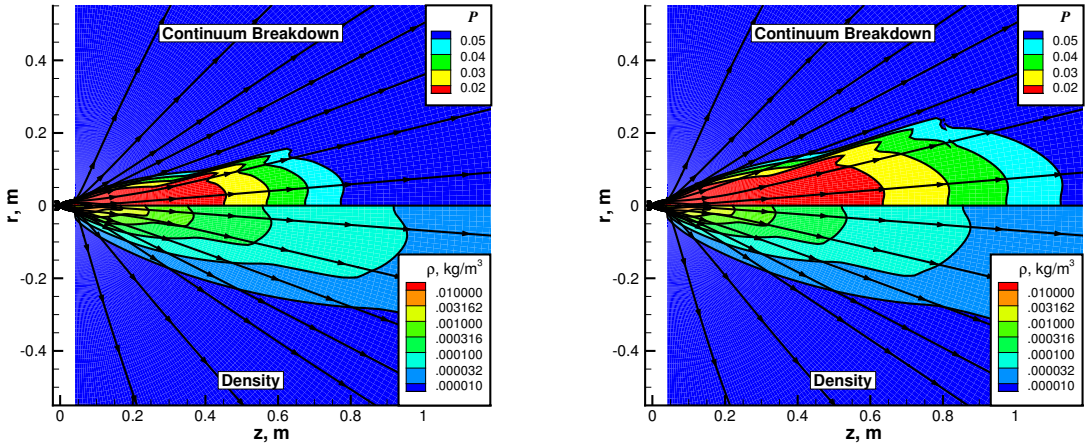

a) Expanding perfect gas jet (N_2).

b) Expanding hydrazine reaction gas jet (NH_3-N_2-H_2 mixture).

Figure 6. CFD flow field of supersonic nozzle (DPLR [29]).

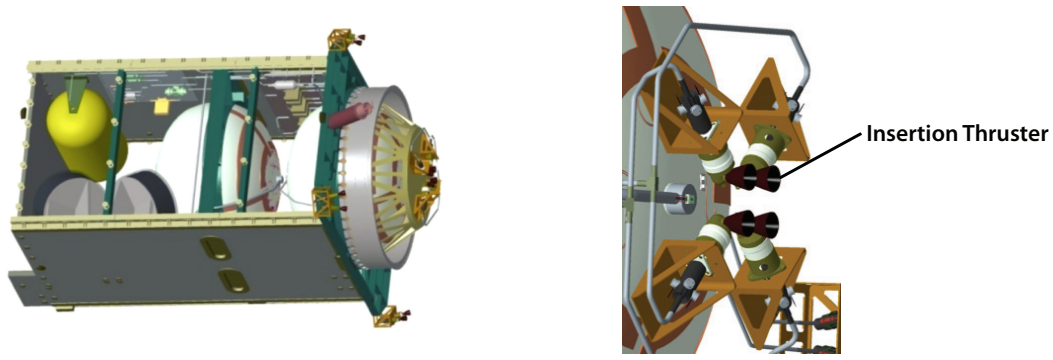

a) Full view of LRO (Note: thrusters on right end).

b) Close-up view of four tightly-clustered insertion thrusters.

Figure 7. Schematic of Lunar Reconnaissance Orbiter (LRO) internal propulsion components.

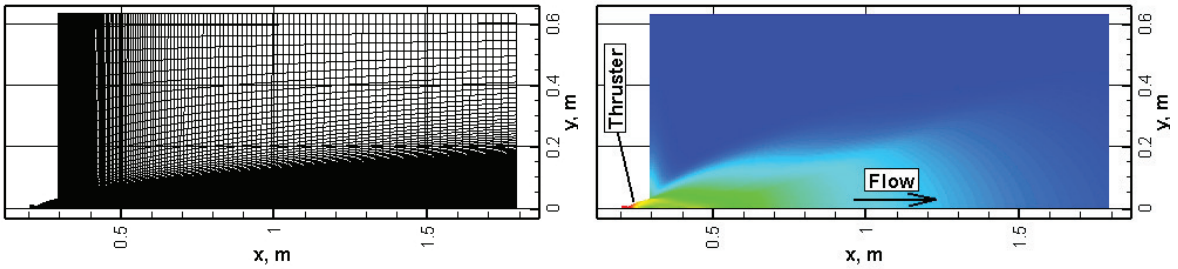

a) Axisymmetric grid for insertion thruster.

b) Axisymmetric flow field solution for insertion thruster.

Figure 8. LRO insertion thruster nozzle and external flow field CFD.

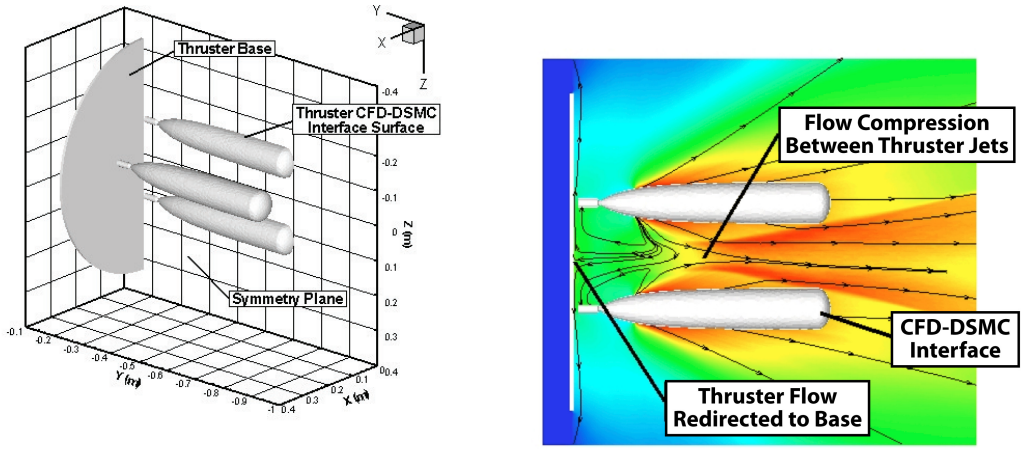

a) DSMC simulation regime and boundary conditions.

b) DSMC flow field solution.

Figure 9. LRO insertion thruster interaction DSMC boundaries and flow field.

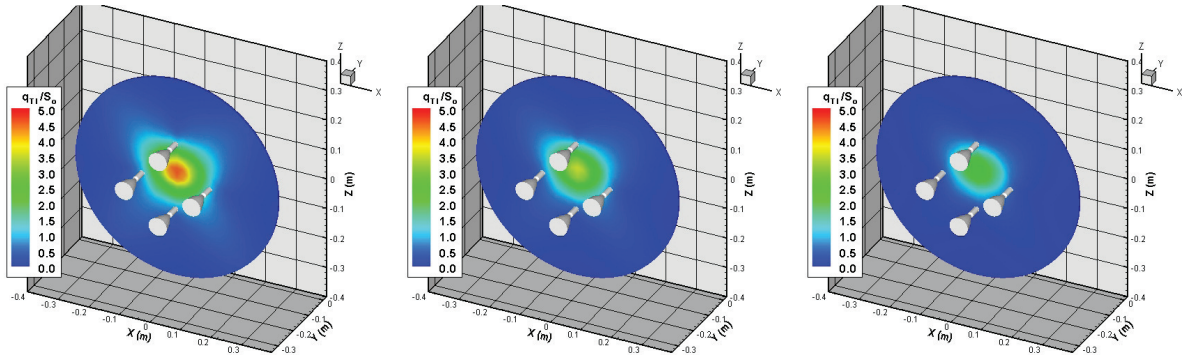

a) **Thruster base** $T_{wall} = 100$ K.

b) **Thruster base** $T_{wall} = 300$ K.

c) **Thruster base** $T_{wall} = 500$ K.

Figure 10. LRO thruster base plate heating from insertion jet interaction reverse flow.

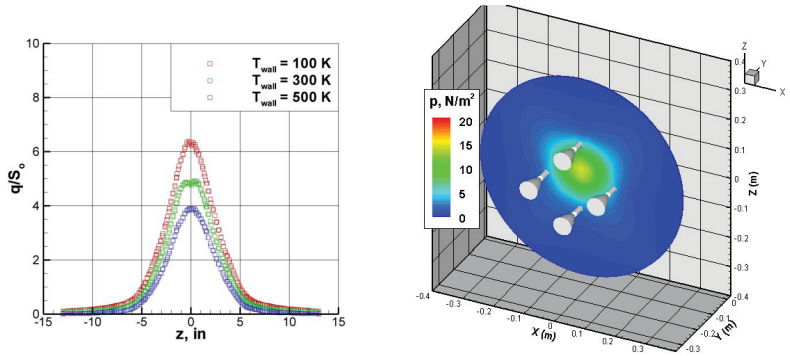

a) Surface heating loads on base plate. b) Surface pressure loads on base plate.

Figure 11. LRO insertion thruster interaction heating and pressure loads on base plate.

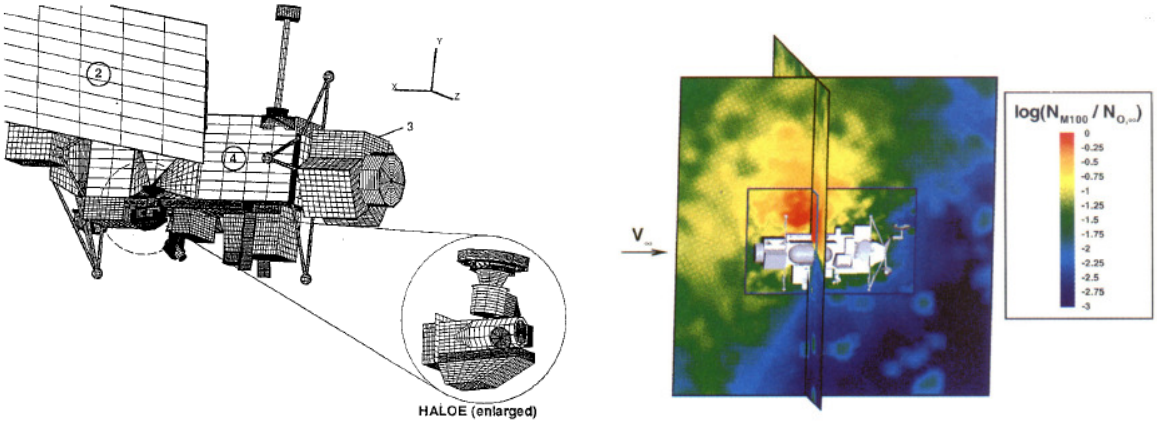

a) Surface grid. b) Free stream contamination of heavy outgassed molecules.

Figure 12. DSMC of UARS with HALOE telescope optics RCS plume contamination (taken from [38]).

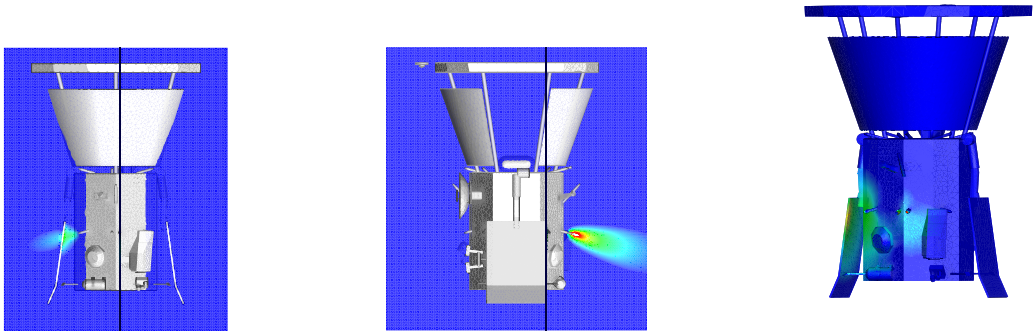

a) RL-1 ACS flow field. b) RL-2 ACS flow field. c) Surface contamination from ACS plume.

Figure 13. DSMC of Solar Probe Plus Attitude Control System (ACS) plume contamination.

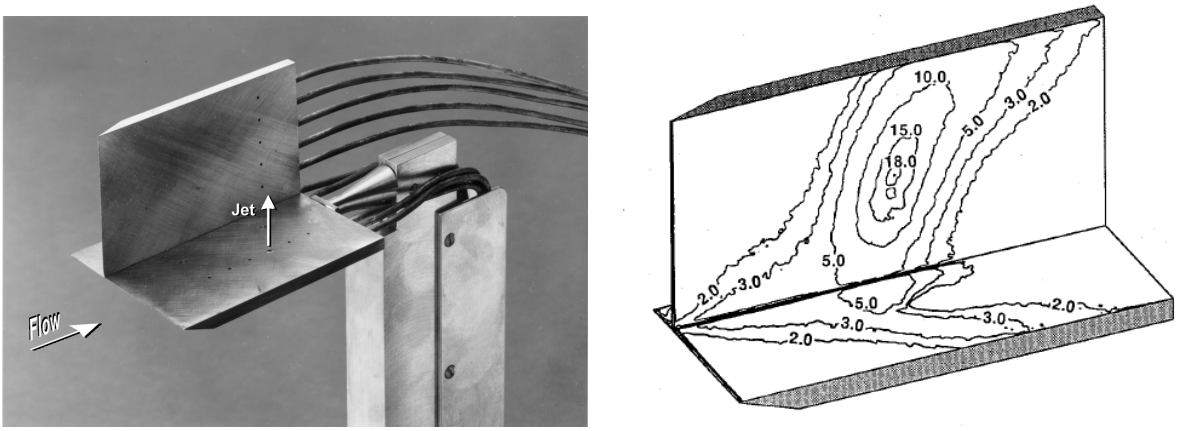

a) Experimental setup [43] b) DSMC surface pressure [10]

Figure 14. Jet interaction corner flow model of Allègre and Raffin [43].

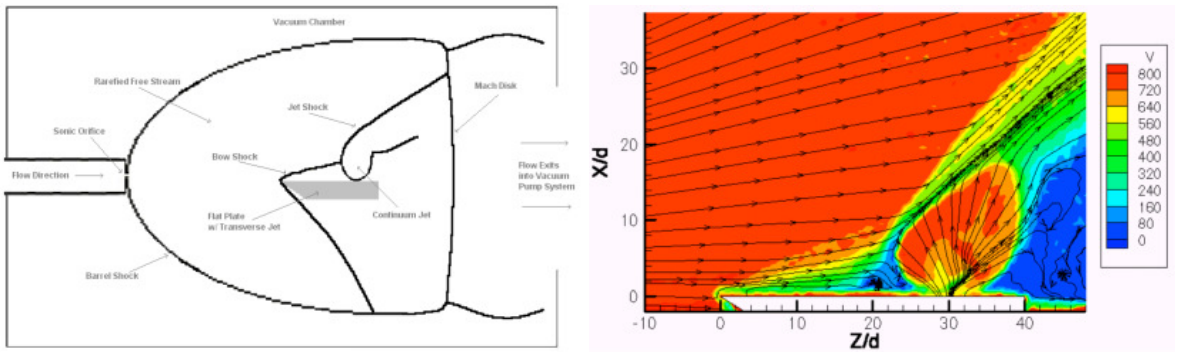

a) Sketch of RCS model. b) Experimental velocity contours

Figure 15. UVA rarefied free stream RCS jet interaction experiment.

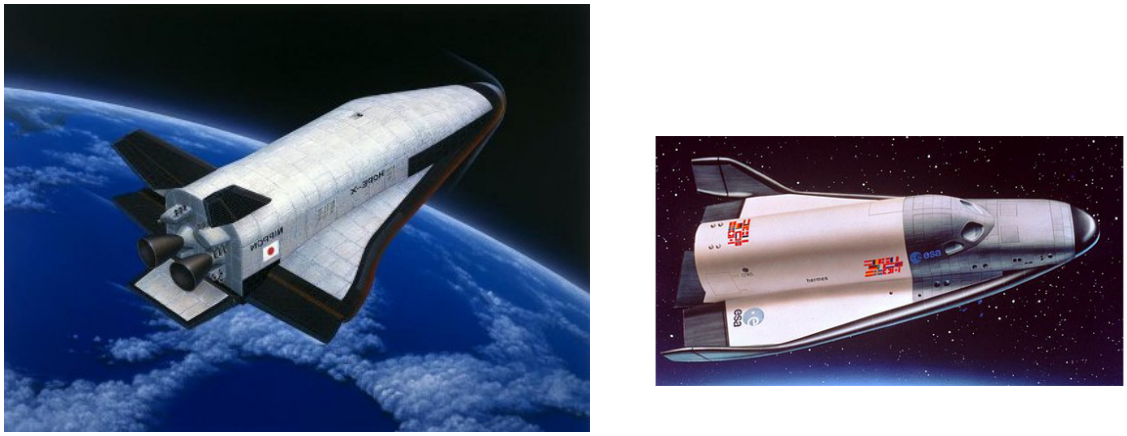

a) JAXA HOPE-X [68]. b) ESA HERMES [69].

Figure 16. Space vehicle configurations studied internationally to assess RCS jet interaction effects.

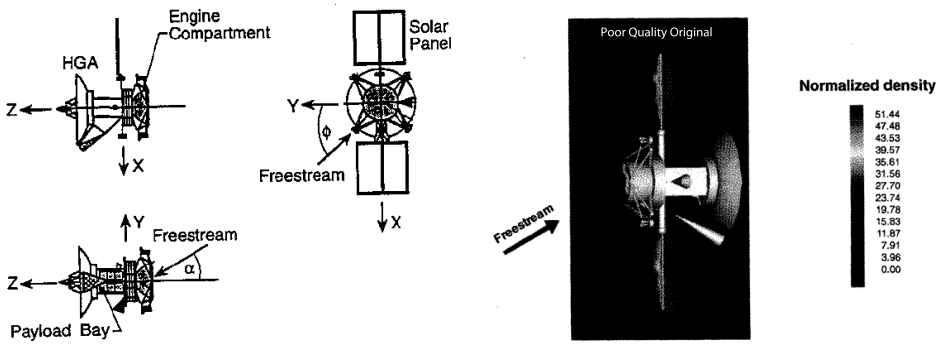

a) Magellan reference frame. b) Free stream density from DSMC.

Figure 17. DSMC simulation of Magellan (taken from [61]).

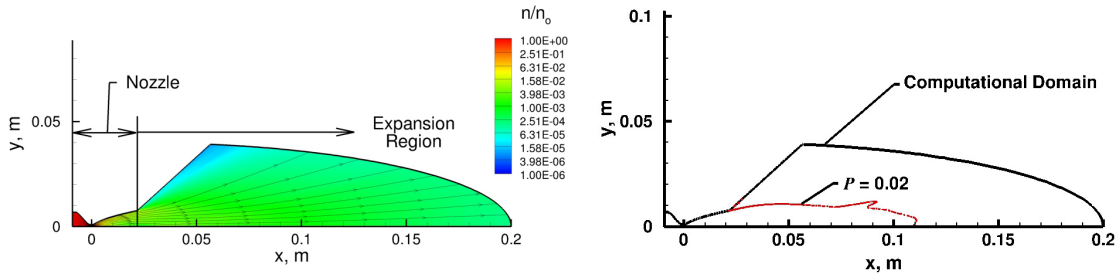

a) Computational domain of nozzle and expanding jet. b) Thruster continuum breakdown ($P = 0.02$ outlined red).

Figure 18. CFD flow field of MGS ACS thruster supersonic nozzle.

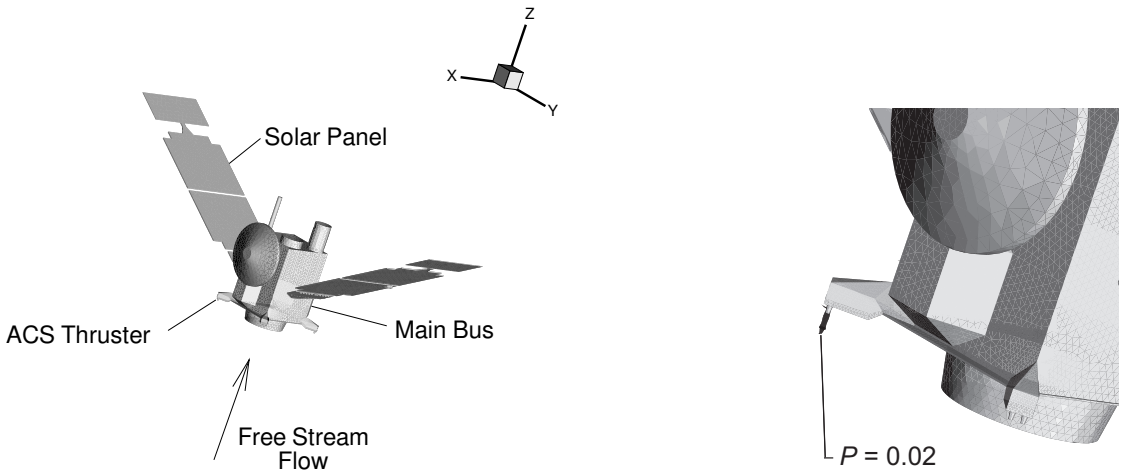

a) Orientation during aerobraking pass. b) Close-up view of Bird breakdown surface.

Figure 19. Schematic of MGS and ACS thuster continuum breakdown surface.

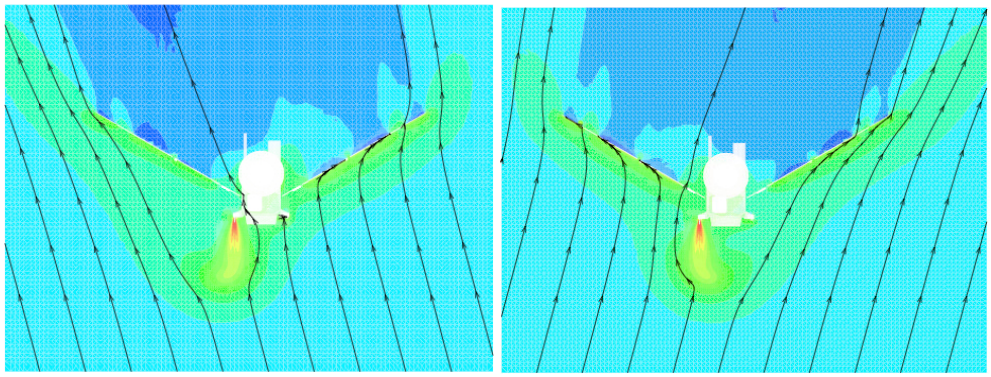

a) $\alpha = -15°$. **b)** $\alpha = 15°$.

Figure 20. MGS ACS jet interaction density contours from uncoupled CFD-DSMC simulation.

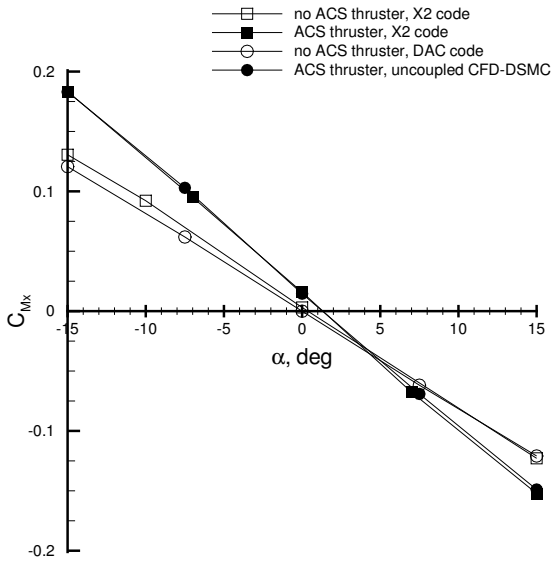

Figure 21. Yawing moment coefficient as a function of α for MGS from ACS jet interation.

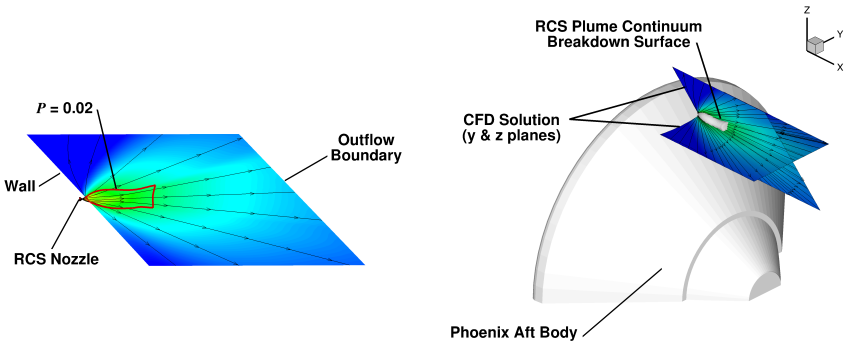

a) CFD Planar Cut (*P* = 0.02 red). b) Continuum breakdown surface.

Figure 22. CFD of Phoenix RCS Thruster.

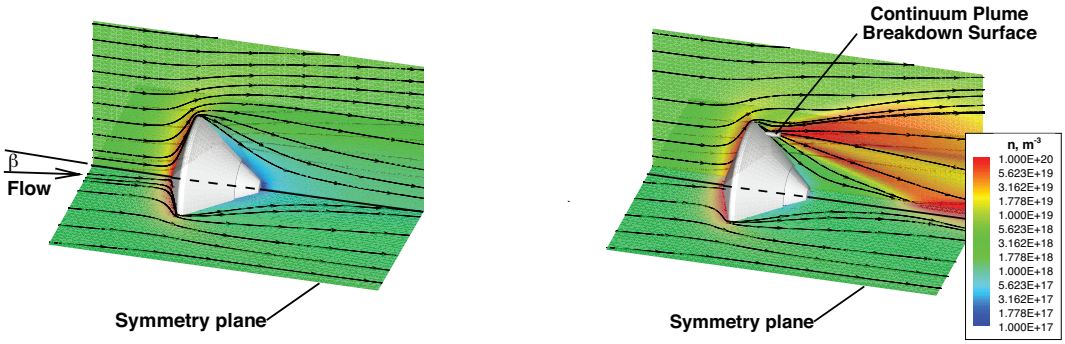

a) No RCS thruster. b) With RCS thruster.

Figure 23. DSMC of Phoenix flow field at $Kn_L = 0.1$.

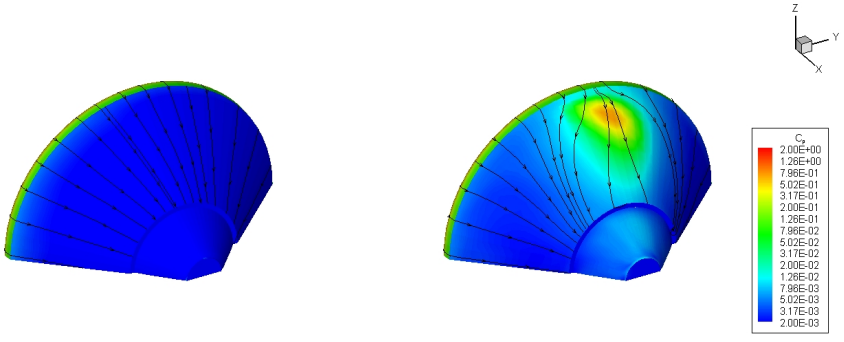

a) Surface pressure without RCS thruster. b) Surface pressure with RCS thruster.

Figure 24. DSMC of Phoenix afterbody at $Kn_L = 0.1$.

REPORT DOCUMENTATION PAGE

Form Approved
OMB No. 0704–0188

1. REPORT DATE *(DD-MM-YYYY)*	2. REPORT TYPE	3. DATES COVERED *(From - To)*
01-10-2018	Technical Publication	

4. TITLE AND SUBTITLE
Numerically Simulating an Expanding Continuum Jet into a Surrounding Non-continuum Region

5a. CONTRACT NUMBER

5b. GRANT NUMBER

5c. PROGRAM ELEMENT NUMBER

6. AUTHOR(S)
Christopher E. Glass

5d. PROJECT NUMBER

5e. TASK NUMBER

5f. WORK UNIT NUMBER
432938.11.01.07.43.40.05

7. PERFORMING ORGANIZATION NAME(S) AND ADDRESS(ES)
NASA Langley Research Center
Hampton, Virginia 23681-2199

8. PERFORMING ORGANIZATION REPORT NUMBER
L–20905

9. SPONSORING/MONITORING AGENCY NAME(S) AND ADDRESS(ES)
National Aeronautics and Space Administration
Washington, DC 20546-0001

10. SPONSOR/MONITOR'S ACRONYM(S)
NASA

11. SPONSOR/MONITOR'S REPORT NUMBER(S)
NASA–TP–2018–220095

12. DISTRIBUTION/AVAILABILITY STATEMENT
Unclassified-Unlimited
Subject Category 64
Availability: NASA STI Program (757) 864-9658

13. SUPPLEMENTARY NOTES
An electronic version can be found at http://ntrs.nasa.gov.

14. ABSTRACT

A numerical technique that simulates the interaction between a continuum jet and a free-molecular, rarefied or transitional flow field is presented and applied. The technique is based on selecting a boundary between the expanding jet plume and interacting flow field defined by the Bird breakdown parameter, P. By properly choosing the boundary, the jet plume computed by computational fluid dynamics (CFD) is uncoupled from the interaction region that is simulated by direct simulation Monte Carlo (DSMC). The mechanics of uncoupling the continuum and non-continuum regions is discussed first. Also, a discussion of expanding continuum plume breakdown and the formulation of the Bird breakdown parameter is presented. To show the usefulness, examples of applying the CFD–DSMC technique are given. Many of the examples were taken from projects worked by the staff of the Aerothermodynamics Branch at the NASA Langley Research Center. These examples show a variety of applications of the technique and allow those examples not previously documented to be formally presented.

15. SUBJECT TERMS
DSMC, CFD, continuum breakdown, jet interaction

16. SECURITY CLASSIFICATION OF:			17. LIMITATION OF ABSTRACT	18. NUMBER OF PAGES	19a. NAME OF RESPONSIBLE PERSON
a. REPORT	b. ABSTRACT	c. THIS PAGE			STI Help Desk (email: help@sti.nasa.gov)
U	U	U	UU	42	19b. TELEPHONE NUMBER *(Include area code)* (757) 864-9658